Applied Energy 368 (2024) 123476

Contents lists available at ScienceDirect

Applied Energy

journal homepage: www.elsevier.com/locate/apenergy

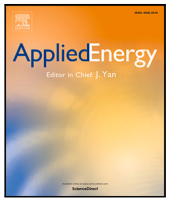

Thermodynamic assessment of an iron-based circular energy economy for carbon-free power supply

Jannik Neumann [a,*], Quentin Fradet [b], Arne Scholtissek [c], Frank Dammel [a], Uwe Riedel [b], Andreas Dreizler [d], Christian Hasse [c], Peter Stephan [a]

[a] Technical University of Darmstadt, Department of Mechanical Engineering, Institute for Technical Thermodynamics, Peter-Grünberg-Straße 10, 64287 Darmstadt, Germany
[b] German Aerospace Center (DLR), Institute of Low-Carbon Industrial Processes, Walther-Pauer-Straße 5, 03046 Cottbus, Germany
[c] Technical University of Darmstadt, Department of Mechanical Engineering, Simulation of Reactive Thermo-Fluid Systems, Otto-Berndt-Straße 2, 64287 Darmstadt, Germany
[d] Technical University of Darmstadt, Department of Mechanical Engineering, Reactive Flows and Diagnostics, Otto-Berndt-Straße 3, 64287 Darmstadt, Germany

GRAPHICAL ABSTRACT

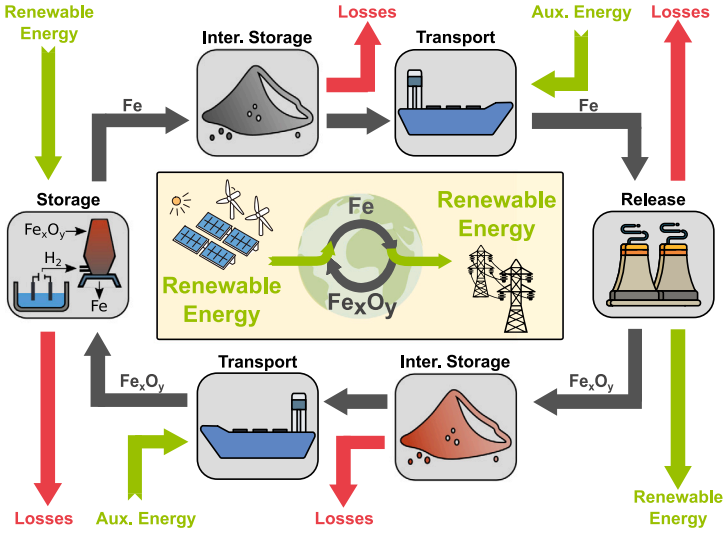

ARTICLE INFO

Keywords:
Chemical energy carrier
Metal fuels
Iron-based energy cycle
Power-to-power efficiency
Hydrogen direct reduction
Iron-fired power plants

ABSTRACT

As the urgency for decarbonization of economies around the world is becoming more pressing, green energy carriers synthesized with renewable energy are emerging as tradable commodities for connecting regions with abundant renewable energy to those with high energy demand. Among the various options, metals – especially iron – have been identified by the scientific community as promising green fuels due to their high volumetric energy densities. However, there persists a gap in comprehensive thermodynamic analyses despite the growing interest. This study provides a rigorous thermodynamic assessment of an iron-based circular energy economy for carbon-free power supply. The circular system encompasses the storage of renewable energy through the thermochemical reduction of iron oxide powder to metallic iron powder, intermediate storage, energy release in iron-fired power plants via thermochemical oxidation of the iron powder, and long-distance inter-regional

* Corresponding author.
E-mail address: neumann@ttd.tu-darmstadt.de (J. Neumann).

https://doi.org/10.1016/j.apenergy.2024.123476
Received 28 November 2023; Received in revised form 5 April 2024; Accepted 12 May 2024
Available online 25 May 2024

transport. Each sub-process of the iron-based energy cycle is described and evaluated using comprehensive thermodynamic models, addressing technical implications and thermodynamic limitations. Two technological options for the hydrogen direct reduction of iron oxides – namely, the shaft furnace and the flash reactor hydrogen direct reduction – are compared. The thermodynamic assessments reveal that the flash reactor is superior to the shaft furnace concept, primarily due to the elimination of additional process steps for particle size adjustments. Moreover, the study underscores the feasibility of iron-fired power plants as a means to retrofit and decarbonize existing coal-fired power plants. The analysis shows that iron-fired power plants attain higher efficiency levels than coal-fired power plants, even under non-ideal conditions. Regarding transport, industrial practices and regulations for handling iron and its oxides are well established globally, providing further confidence in the feasibility of the approach. The findings indicate that integrating an iron-based circular energy economy with the repurposing of existing infrastructure presents a compelling option. This approach effectively addresses the temporal and spatial mismatch between energy demand and supply serving as a critical enabler for renewable energy transport and long-term storage, which is essential for a successful energy transition.

Nomenclature

Abbreviations

AYR	Adiabatic yield reactor
CFD	Computational fluid dynamics
CFPP	Coal-fired power plant
DRI	Direct reduced iron
EC	Energy carrier
EAF	Electric arc furnace
FGD	Flue gas desulfurization
FGR	Flue gas recirculation
FR	Flash reactor
GOD	Gas oxidation degree
HDR	Hydrogen direct reduction
HEX	Heat exchanger
IFPP	Iron-fired power plant
IIMA	Internat. Iron Metallics Association
IMO	Internat. Maritime Organization
IMSBC	Internat. Maritime Solid Bulk Cargoes
IYR	Isothermal yield reactor
MW	Molecular weight
RE	Renewable energy
SF	Shaft furnace
TRL	Technological readiness level

Symbols

d	Distance, m
E	Energy, J
EE	Elementary effect
h	Specific enthalpy, $\mathrm{J\,kg^{-1}}$
H_R	Reaction enthalpy, $\mathrm{J\,mol^{-1}}$
HV	Heating value, $\mathrm{J\,kg^{-1}}$
LHV	Lower heating value, $\mathrm{J\,kg^{-1}}$
m	Mass, kg
$\dot{m}$	Mass flow rate, $\mathrm{kg\,s^{-1}}$
N	Molar amount, mol
p	Pressure, bar
$\dot{Q}$	Heat flow, W
P	Power, W
T	Temperature, °C
X	Degree of oxidation/reduction
x	Mass fraction
y	Molar fraction

Greek symbols

α	Relative peripheral losses
β	Relative boiler losses
γ	Relative auxiliary losses
Δ	Difference
ϵ	Effectiveness
η	Efficiency
λ	Equivalence ratio
μ	Mean
σ	Standard deviation
ϕ	Step size
ω	Increment

Subscripts

ato	Atomization
aux	Auxiliary
b	Boiler
comb	Combustion
cond	Condenser
cyc	Cycle
ely	Electrolysis
env	Environment
f	Fuel, formation
fg	Flue gas
fh	Fuel handling
is	Intermediate storage
isn	Isentropic
mat	Material
ms	Main steam
misc	Miscellaneous
net	Net
ox	Oxidation
pel	Pelletization
per	Peripheral
R	Reactor
recov	Recoverable
red	Reduction
rel	Release, relative
rep	Reproduction
rs	Reheated steam
sto	Store
s	Steam
sl	Slag

tg	Turbine/generator
tot	Total
tra	Transport
u	Unburned

Chemical symbols

C	Carbon
CO	Carbon monoxide
CO_2	Carbon dioxide
Fe	Iron
Fe_zO	Wüstite
Fe_3O_4	Magnetite
Fe_2O_3	Hematite
Fe_xO_y	Mixture of iron (oxides)
H_2	Hydrogen
H_2O	Water
N_2	Nitrogen
NO_x	Nitrogen oxides
O_2	Oxygen

1. Introduction

The substantial emissions of greenhouse gases that result from the use of fossil fuels require rapid, substantial, and sustained reductions to mitigate the intensifying adverse impacts on our climate [1], particularly on vulnerable populations [1–3]. Governments worldwide are confronted with the challenge of ensuring energy security, meeting the growing demand for energy, and concurrently reducing greenhouse gas emissions. This transition to clean energy requires a significant increase in the utilization of renewable energy (RE) sources and end-use electrification [4]. Despite a vigorous expansion of RE, accounting for 90% of the global growth in electricity in 2022 [5,6], the rise in emissions from coal led to a 0.9–1.3% net increase in global energy-related CO_2 emissions [5,6], reaching a new peak. Global coal-based power generation accounts for approximately 10.2 PW h in 2022, constituting 36.6% of global power generation, making it the world's primary source of electricity [6]. The global operating capacity of coal-fired power plants (CFPPs) is around 2.1 TW [7], with the majority of operating plants being less than 20 years old [7]. Additionally, about 0.5 TW are currently announced, permitted, or under construction [7]. These plans stand in contrast to the resolution of the 2015 Paris Climate Change Conference [8], which aims to limit global warming to 1.5 °C (at most 2 °C), and the recent agreement from the 26th United Nations Climate Change Conference (COP 26) [9], at which an acceleration of the phase down of CFPP was concluded by a relevant group of countries. Consequently, given the typical 50 year lifespan of CFPPs, many power plants are to be decommissioned well before their end of life leading to assets worth trillions of dollars becoming obsolete. This scenario offers an opportunity to re-purpose this soon-to-be idle infrastructure by retrofitting the power plants for carbon-free electricity generation with green iron. Moreover, due to the inherent intermittency of RE sources, the development of a secure and decarbonized power sector requires a much larger-scale controllable green power supply than currently exists [10–13]. As a characteristic example, Germany illustrates the broader energy storage limitations faced by many developed nations. If Germany was to meet its average power demand solely with its existing energy storage facilities, such as pumped hydroelectric (24 GWh in 2023 [14]) and battery storage (11 GWh in 2023, mainly small home battery storage systems [14]), these energy storage facilities would be depleted in roughly forty minutes (based on the 2023 grid load of 457 TWh [15]). This constraint is not unique to Germany; other European countries and also Japan face similar challenges. Various geographical, sociological, or technological factors limit these nations' potential for energy self-sufficiency. In Germany's case, imports accounted for 76% of its total primary energy supply in 2022 [16], and projections suggest that it will remain a net energy importer in the foreseeable future [17]. Against this backdrop, chemical energy carriers (ECs), synthesized using RE sources, present a viable solution for connecting regions with abundant RE to low-cost production sites and end-users of green ECs via global value chains [12,13,18,19]. In this respect, hydrogen and hydrogen-based ECs have been widely recognized as potential means to bridge this gap, as supported by several assessments [20–26], international strategies and collaborations [27–30] as well as funding programs [31,32].

Metal fuels, particularly iron, are a promising alternative due to their exceptional volumetric energy densities, favorable storage, and transport characteristics [33–38]. Recent studies have confirmed iron's potential, including initial techno-economic assessments [39–41]. The iron-based energy cycle involves the thermochemical reduction of iron oxides with green hydrogen, allowing electrical energy from renewable sources to be stored chemically as iron. The stored energy can be converted back into electricity by thermochemical oxidation in retrofitted CFPP [42]. A process scheme of this iron reduction-oxidation cycle is shown in Fig. 1. This approach holds great potential for contributing to the required on-demand power generation and offers a cost-effective route to rapid implementation through the reuse of existing infrastructure. Furthermore, synergy effects with developments in the steel industry towards sustainable steel production [43–51] can be utilized for the regeneration of the iron oxides. Finally, transporting the iron oxides back to the reduction sites is necessary to close the cycle. Unlike hydrogen-derived ECs, no water is exported from the production sites since no molecular components of water are bound to iron. This can be a decisive criterion for potential exporters of green ECs with water scarcity [52].

While there is growing interest in the use of iron as an EC, the literature still offers a limited number of cycle analyses [37,39,53,54]. Dirven et al. [53] conducted an initial estimation of power-to-power efficiency, which includes release, storage, and transport, and found an efficiency of approximately 20%. Debiagi et al. [37] estimated the complete cycle efficiency to be in the range of 26% to 31%, while Neumann and da Rocha et al. [39] computed a power-to-power efficiency of 16% to 29%, which includes long-distance transport. On the other hand, Kuhn et al. [54] performed an initial assessment using simplified process models, incorporating both thermodynamic (i.e. thermodynamic equilibrium) and physical (i.e. melting point of iron/iron oxides) constraints, leading to a cycle efficiency of 27%, neglecting transport losses. Specific assumptions regarding these efficiency estimations can be found in Table 1.

Prior research offers initial efficiency estimates for iron as an EC for carbon-free electricity generation. However, these estimates are subject to considerable uncertainties due to limited details in the modeling of sub-processes. The objective of this study is to improve and refine these initial cycle assessments by developing comprehensive thermodynamic models that evaluate the oxidation process in iron-fired power plants (IFPPs) for carbon-free electricity generation, and the thermochemical reduction process in shaft furnace and flash reactor plants with green hydrogen for the regeneration of iron oxides, taking into account required pre- and post-treatment steps (i.e. pelletization and atomization). The models are interconnected through transport and intermediate storage, which may lead to losses such as partial oxidation of the iron. Through the evaluation of these individual models, as well as the overarching interconnected model, sub-process efficiencies and overall power-to-power-efficiency is quantified. Further, constraints, potential bottlenecks, as well as essential operation parameters are identified.

To achieve the stated objective, the manuscript is structured into eight main sections. The applied methods and computational tools

Table 1
Compilation of relevant efficiency estimates with respect to the presented iron-based energy cycle for carbon free electricity generation and thermochemical reduction of iron oxides with green hydrogen.

Storage		Release	Transport	Cycle	Comment	Reference
Electrolysis	Reduction					
70%	91%	43%	–	27%	No transport losses	[54]
70–80%	80%	50%	93–96%	26–31%	≈3000 km transport distance	[37]
46–60%		46–50%	91–99%	16–29%	3000–18 000 km transport distance	[39]
≈55%		≈38%	94–99%	≈20%	1000–10 000 km transport distance	[53]

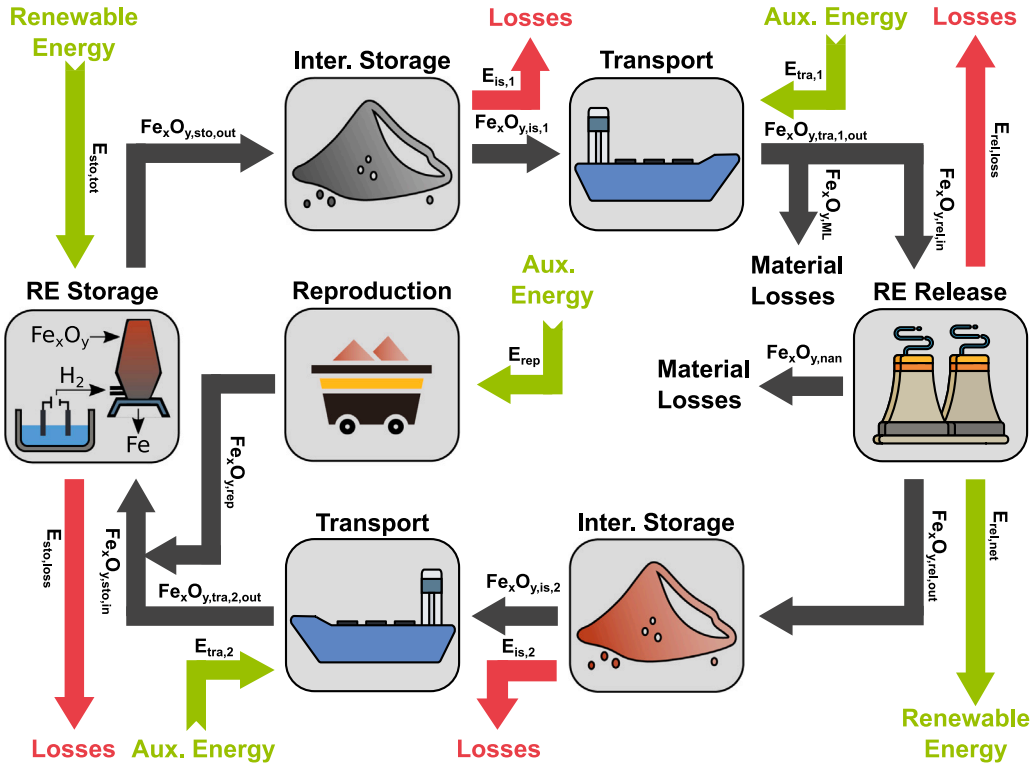

Fig. 1. Schematic of an iron reduction-oxidation cycle for renewable energy storage and release for carbon-free electricity generation, including intermediate storage, reproduction, and transport of the iron (oxides).

used are briefly outlined in Section 2. Thermodynamics and technological options relevant to the hydrogen direct reduction of iron oxides are discussed in Section 3. In Section 4, the iron oxidation process and strategies for adapting existing CFPPs to iron operation is presented. The interlinking sub-processes, including intermediate storage, transport, and other handling aspects, are discussed in Section 5. Within Section 6, metrics for assessing the performance are introduced. Building on the previous sections, in Section 7 both the individual sub-processes and the overarching iron-based energy cycle are evaluated and discussed. The manuscript ends with a comprehensive conclusion that summarizes the main findings and implications.

2. Methods

For the in-depth analysis, comprehensive thermodynamic models are developed with the process modeling software EBSILON® *Professional* [55], which offers an extensive library of process components and material data for working fluids and fuels. Accounting for thermodynamic state changes, mixing/separation, and chemical reactions, the software is used to solve mass and energy balances for all interlinked sub-processes. NASA polynomials [56] for the thermodynamic properties of relevant species are already built into the software. Most of the relevant process units are predefined and available in EBSILON, while user-defined models for the reaction units are implemented. The sub-process models are linked within the EBSILON framework, resulting in an overarching cycle model that is solved for stationary conditions. To construct phase diagrams and investigate thermodynamic equilibria for the reaction systems, the thermochemical software and database package FactSage [57], is employed. These thermodynamic constraints are then integrated into the sub-process models within EBSILON. For a detailed assessment of individual sub-processes and the overarching energy cycle, several efficiencies are defined and added as performance indicators to the model. Lastly, local and Morris sensitivity analyses are performed, which serve as approximations for global process sensitivities of target quantities with respect to input variables. All sub-process models are parameterized carefully, and the underlying assumptions and validation cases are detailed in subsequent sections.

3. Storage: Hydrogen direct reduction

This section provides background on the governing reactions and equilibrium limitations for the reduction of iron oxides with green hydrogen (hydrogen direct reduction, HDR). Features of co-current and counter-current reactor setups are briefly discussed and two promising direct reduction concepts, i.e. shaft furnace hydrogen direct reduction (SF-HDR) and flash reactor hydrogen direct reduction (FR-HDR), are introduced.

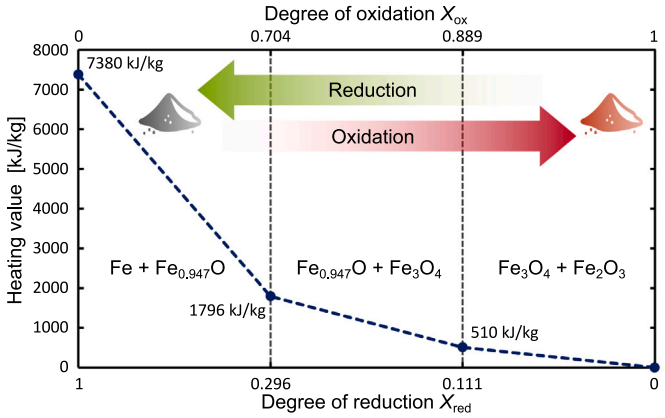

Fig. 2. Resulting heating value of iron as function of reduction degree, assuming a step-wise reduction/oxidation. Note the non-equidistant scaling of the abscissa.

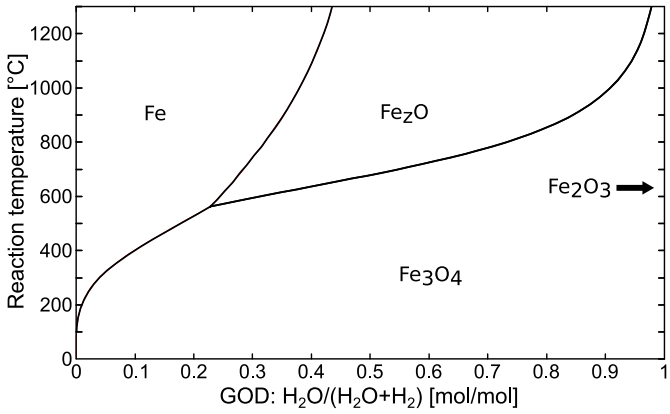

Fig. 3. Baur-Glässner diagram for the Fe–O–H system. The diagram was derived using FactSage 8.2 [57], utilizing the FactPS and FTOxid databases.

3.1. Thermodynamics of hydrogen direct reduction

The global crude steel production contributes to approximately 7% of worldwide carbon dioxide (CO_2) emissions [58]. This substantial contribution mainly stems from the primary steelmaking route, i.e. with iron ore as main input; a production route traditionally reliant on coal. In particular, a large share of the emissions arises from the ironmaking step in blast furnaces. Coke is oxidized to generate heat and carbon dioxide, which is in turn converted into carbon monoxide (CO) through the Boudouard reaction. Carbon monoxide is the main reducing agent in blast furnaces that converts iron oxides, typically hematite (Fe_2O_3), into elemental iron (Fe), as illustrated in Eq. (1):

$$Fe_2O_3 + 3\,CO \rightarrow 2\,Fe + 3\,CO_2 \quad \Delta H_R(25\ ^\circ C) = -23.6\,kJ\,mol^{-1}\,. \tag{1}$$

However, the use of natural/synthesis gas in shaft furnaces for solid-state reduction presents a promising alternative, particularly in regions with access to low-cost natural gas. This so-called direct reduction process significantly reduces the CO_2 emissions (i.e. by 40-60% [59]) associated with ironmaking. Moreover, green-hydrogen ironmaking aims at fully replacing carbon monoxide as reducing agent with hydrogen (H_2), which emits water (H_2O) instead of CO_2 as a byproduct as shown in Eq. (2):

$$Fe_2O_3 + 3\,H_2 \rightarrow 2\,Fe + 3\,H_2O \quad \Delta H_R(25\ ^\circ C) = 98.8\,kJ\,mol^{-1}\,. \tag{2}$$

The global reaction (Eq. (2)) is a stepwise process, which proceeds above 843 K from hematite to magnetite (Fe_3O_4, Eq. (3)), then to wüstite (Fe_zO, Eq. (4)), and finally to metallic iron (Eq. (5)) [60]. The non-stoichiometric iron monoxide wüstite can exist in different modifications due to point and cluster defects and pseudo-phases ($z \in [0.96 - 0.82]$) [61]. Based on the applied thermodynamic data [56], it is assumed that wüstite only exists as $Fe_{0.947}O$ ($z = 0.947$):

$$Fe_2O_3 + 1/3\,H_2 \rightarrow 2/3\,Fe_3O_4 + 1/3\,H_2O\,, \tag{3}$$

$$z\,Fe_3O_4 + (4z-3)\,H_2 \rightarrow 3\,Fe_zO + (4z-3)\,H_2O\,, \tag{4}$$

$$Fe_zO + H_2 \rightarrow z\,Fe + H_2O\,. \tag{5}$$

The progression of the reduction (and oxidation) can be quantified with a degree of reduction (oxidation) X_{red} (X_{ox}) [62], which is given by

$$X_{red} = 1 - X_{ox} = 1 - \frac{N_{O,bound}}{1.5 \cdot N_{Fe,total}}\,, \tag{6}$$

where $N_{Fe,total}$ represents the molar amount of iron and $N_{O,bound}$ corresponds to the molar amount of oxygen bound to the iron.

For the modeling and evaluation of the sub-processes and the overarching cycle, the stored energy within the iron (oxides) is an important criterion, which is quantified by the heating values (HVs) of the corresponding iron and its oxides. Fig. 2 displays the heating value as a function of the previously introduced reduction degree, assuming a stringent stepwise reaction (i.e. reactions (3), (4), (5)). It becomes clear that most of the stored energy is available by the reaction of iron to wüstite, and only a small amount of the total available energy is accessible within the last reaction from magnetite to hematite. Table 2 provides further details on the thermochemical data, such as melting points and HV of iron and its oxides.

Fig. 3 presents the Baur-Glässner diagram [63,64], which depicts the Fe–O–H system. This diagram displays the stability regions of iron and its oxides as a function of temperature and gas oxidation degree (GOD). It is evident that the stability areas of iron and wüstite increase with rising temperature and declining GOD. For example, at reaction temperatures of 700 °C and 900 °C, having GODs lower than 29% and 35%, respectively, is a necessary condition to ensure the stability of iron. However, this diagram only depicts the thermodynamic equilibrium, giving a certain temperature and GOD. In practical applications, the gas composition evolves, so that a hydrogen surplus is needed to achieve complete conversion to iron, especially for a co-current setup. The available hydrogen is quantified in the hydrogen equivalence ratio:

$$\lambda_{H_2} = \frac{\text{available hydrogen quantity}}{\text{stoichiometric required hydrogen quantity}}\,,$$

$$\lambda_{H_2} = \frac{N_{H_2}}{3 \cdot N_{Fe_2O_3} + 4 \cdot N_{Fe_3O_4} + 1 \cdot N_{Fe_zO}} \left[\frac{mol}{mol}\right]. \tag{7}$$

Fig. 4 illustrates the minimum combinations of reaction temperature and hydrogen equivalence ratio necessary for complete conversion to iron (i.e. $X_{red} = 1$) assuming a co-current flow reactor concept (i.e. flash reactor concept) for different GODs at the inlet of the reactor, forming a Pareto front. For instance, at a GOD of zero and reaction temperatures of 700 °C and 900 °C, hydrogen equivalence ratios of 3.53 and 2.85 are required, respectively. A GOD of 0.1 necessitates hydrogen equivalence ratios of 4.91 and 3.58. In a counter-current configuration, the theoretical minimum hydrogen amount with a GOD of zero at the gas inlet corresponds to $\lambda_{H_2} = 1$, but it is crucial to note that practical applications may encounter constraints related to reaction kinetics and transport phenomena and also here, a hydrogen surplus is necessary.

3.2. Technological options for ironmaking

Within the framework of the proposed iron-based energy cycle, two HDR concepts, the shaft furnace (SF-HDR) and the flash reactor (FR-HDR), are being further evaluated. The former has been chosen due to its comparatively high technological readiness level (TRL), while the latter is evaluated owing to its ability to process particles sizes that align with the oxidation step of the investigated green iron redox cycle.

Table 2
Thermochemical properties of iron and its oxides [56,57]. The heating values correspond to a complete oxidation to hematite using the given enthalpies of formation $\Delta_f H^0$(25 °C) [56]. Densities are taken from [37].

Name	Molecular formula	MW [g mol^{-1}]	Density [kg m^{-3}]	Melting point [°C]	$\Delta_f H^0$ [kJ mol^{-1}]	HV [kJ kg^{-1}]	X_{ox} [%]	X_{red} [%]
Iron	Fe	55.85	7870	1539	0	7380	0	1
Wüstite	$Fe_{0.947}O$	68.88	5740	1371	−266.27	1796	70.4	29.6
Magnetite	Fe_3O_4	231.53	5180	1597	−1118.38	510	88.9	11.1
Hematite	Fe_2O_3	159.69	5260	NA	−824.25	0	1	0

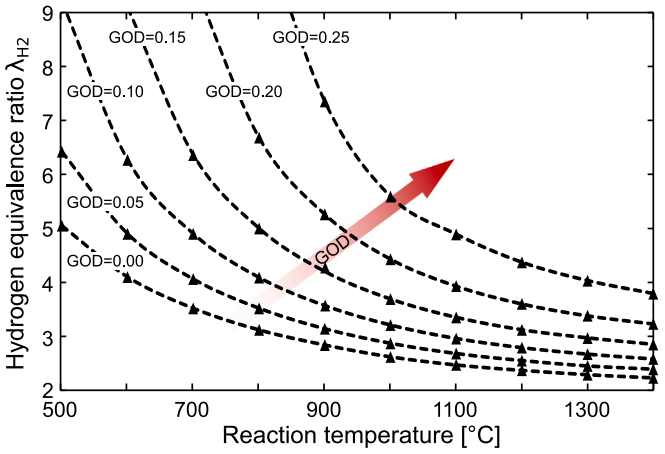

Fig. 4. Mandatory conditions of reaction temperature and hydrogen equivalence ratio vary among different gas oxidation degrees (GODs) at the inlet of an adiabatic reactor to achieve complete conversion to iron for a co-current reactor setup. The diagram was derived using FactSage 8.2 [57], utilizing the FactPS and FTOxid databases.

Among the different reactor concepts for direct reduction [43] aimed at achieving carbon-neutral ironmaking, the shaft furnace process emerges as a highly promising candidate. This process is already operated at an industrial scale [65] with natural gas as reducing agent, and an operation with 100% hydrogen is feasible and currently planned in multiple projects [48,49,66]. However, one limitation of the shaft furnace reduction process in the context of the iron-based energy cycle is the prerequisite of iron oxide pellets as feedstock. These pellets require preparatory processing, which adds additional costs and energy requirements. In order to yield the required fine iron powder for oxidation, the reduced iron pellets must be melted in an energy-intensive electric arc furnace, followed by water-atomizing the melt.

A promising alternative to this concept has been developed by Sohn et al. [50], referred to as flash or suspension ironmaking. The distinguishing feature of this process is its ability to directly utilize fine iron oxide particles, preventing the need for additional pre- and post-treatment. This eliminates the requirement for pelletization and iron powder production, aligning it seamlessly with the described iron-based energy cycle. Further ironmaking concepts are in principle suitable for the iron-based energy cycle. For example, ironmaking processes based on the fluidized bed technology have reached commercial readiness levels and handle iron ore fines directly [67,68]. Nevertheless, these processes require sinter feeds, with particle sizes typically ranging from 0.1 to 2 mm [69]. Recent developments suggest the possibility of handling iron ore ultrafines directly [70,71]. However, the major drawback of the fluidized bed technology in ironmaking applications remains the sticking tendency of the bed, leading to its defluidization [72,73]. Even partial sintering may require post-treatment of the particles for further use in combustion applications. Therefore, flash-based iron making rather than fluidized bed technology is retained for the assessment in the present work.

A radically different ironmaking technology is the electrochemical route. Instead of the intermediate production of hydrogen by water electrolysis and its use in the thermochemical reduction of iron oxide, iron is obtained directly through the electrolysis of iron ore. This technology holds great promise for significantly reducing energy requirements and costs [74–76]. Besides molten oxide electrolysis [77], electrowinning in alkaline [78–80] or acidic [81] media is an attractive option, in particular due to the much lower operating temperatures needed (≈ 100 °C). However, the technology readiness is currently too low, resulting in too large uncertainties for the scope of this work. Subsequently, the two selected processes are described in more detail.

3.2.1. *Shaft furnace hydrogen direct reduction (SF-HDR) and peripheries*

The investigated plant encompassing the pelletization, shaft furnace reduction, water electrolysis, and iron powder production (melting and atomization) is shown in Fig. 5. For each process step, characteristics and significant assumptions are provided subsequently.

Pelletization: The process of iron oxide pelletizing includes three principal stages: the preparation of raw material, the formation of green pellets (referred to as balling), and the induration of green pellets to withstand the thermo-mechanical stresses during the reduction [82–84]. The raw material preparation phase entails the mixing of iron oxides, binders, and water. Bentonite, an inorganic binder predominantly comprised of Al_2O_3, SiO_2, is mixed together with iron oxides and water to fabricate green pellets by balling of the components. The presumed mixture is 90 wt.% iron oxides, 5 wt.% bentonite, and 5 wt.% water, a common ratio in shaft furnace plants [85]. As per Bhagat [82], the induration process consists of four phases: drying (≈ 250 °C), preheating, firing (≈ 1300 °C), and cooling. In cases where iron oxides have not been entirely oxidized ($X_{ox} < 1$), extra heat is emitted until complete oxidation ($X_{ox} = 1$) is attained. This surplus heat aids in the preheating phase, subsequently reducing the energy demand for firing. While conventional fuels such as natural gas, coal, and oil are almost exclusively used today, the induration of pellets can also be fueled by green ECs such as biomass or hydrogen [86]. In this study, green hydrogen has been selected as the firing agent.

Shaft furnace hydrogen direct reduction: Iron oxide reduction via a shaft furnace reactor is a recognized technology that has been globally adopted in numerous plants [87]. Iron oxide pellets, with diameters typically ranging from 10 mm to 15 mm [82], are introduced into the reactor's upper section where they encounter the hot reducing agent, green hydrogen in this case, in a counter flow motion. The sensible heat of the off-gas from the furnace top is utilized in a heat exchanger (hydrogen preheater). A substantial portion of the water present within the cooled off-gas is separated using a downstream condenser. This step is followed by the mixing of the residual hydrogen stream with freshly produced hydrogen from water electrolysis. The resulting hydrogen stream, which still carries some residual water, is fed into the lower part of the reactor. The process concludes with the further processing of the hot iron pellets to produce fine iron powder.

One significant challenge associated with shaft furnace hydrogen direct reduction stems from the absence of an intrinsic energy source. The reduction of iron oxides via hydrogen is endothermic, as illustrated by Eq. (2). This leads to a progressive cooling of the pellets throughout the reactor, possibly leading to insufficient reduction degrees and diminished conversion efficiency due to the need for extended residence times. Various options, without the inclusion of the injection

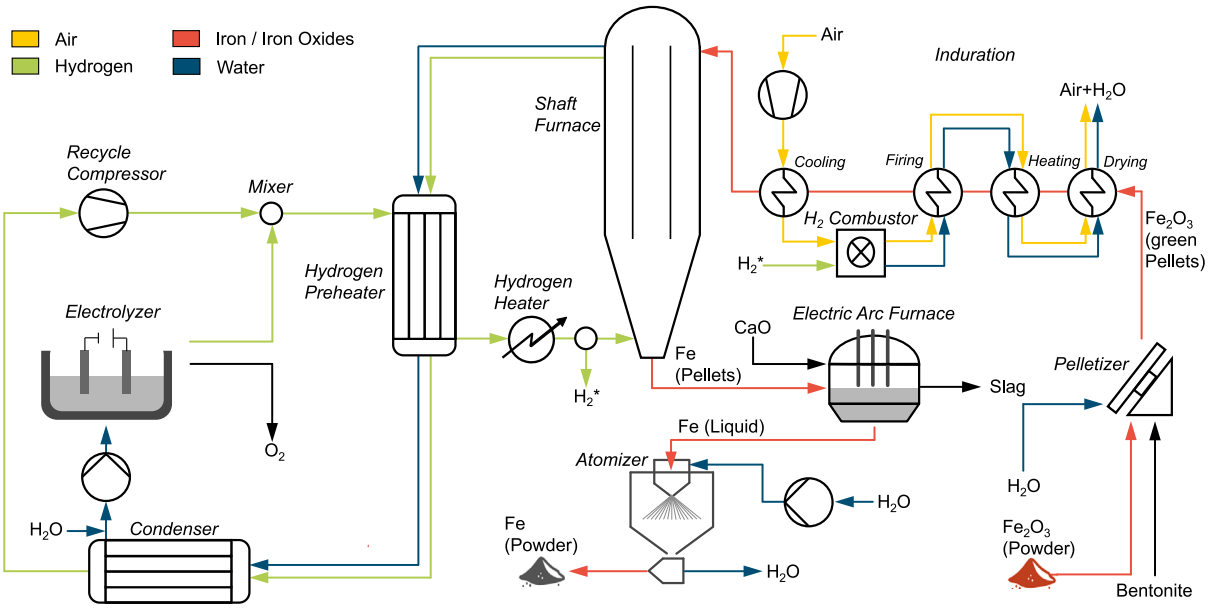

Fig. 5. Schematic of the investigated SF-HDR plant including water electrolysis, and pre- and post-treatment. The cooling cycle for the condenser is not included in the figure.

Table 3
Compilation of recent studies on SF-HDR, presenting their key assumptions and varying scopes. Sensitivity analysis has been conducted in some of these studies [45,88] to assess the impact of different assumptions. The provided values correspond to the reference cases of each study.

Reference			Vogl et al. [44]	Bhaskar et al. [45]	Rechberger et al. [47]	Rosner et al. [88]	This study
Scope	Pelletizer						×
	Shaft furnace		×	×	×	×	×
	Electric arc furnace		×	×		×	×
	Atomizer						×
Reactor inlets	Gas	Temp. [°C]	800	500	980	775	800
		GOD [−]	0	0	0.1	0.02	0.01
	Solids	Temp. [°C]	800	800	NA	25	700
		Inerts [%]	5	5	0	10	5
	H_2 equil. ratio λ_{H_2} [−]		1.5	1.5	≈1.4	1.54	1.5
Reactor outlets	Gas	Temp. [°C]	800	250	NA	351	316
	Solids	Temp. [°C]	800	800	730	700	800
		X_{red} [−]	0.96	0.96	0.95	0.94	1
External heat supply			Elec.	Elec.	NG, H_2	H_2 + O_2 Inj.	Elec. + H_2
Electrolysis efficiency (based on LHV_{H_2})			72%	74%	63%	72%[a]	70%
Reactor modeling approach[b]			IYR	IYR	AYR	AYR	AYR
Total spec. energy demand [MWh t^{-1}]			3.48	3.72	3.73	4.24	3.58

[a] Own assumption since the assessment was performed excluding the electrolyzer.
[b] IYR: Isothermal yield reactor, AYR: Adiabatic yield reactor.

of an external fuel such as natural gas, could mitigate this issue. One such strategy could involve the preheating of the iron oxide pellets introduced to the shaft furnace to counteract the cooling of the pellets. Secondly, operating the process using surplus hydrogen (i.e. large hydrogen equivalence ratios λ_{H_2}), which could serve as a heat carrier. Thirdly, injecting oxygen into the shaft furnace could provide additional heat via the exothermic reaction between oxygen and hydrogen [88]. The emerging significance and growing interest in hydrogen direct reduction in shaft furnaces have motivated the publication of initial assessments [44,45,47,88], which include thermodynamic evaluations of the process. The scope of these studies varies and they propose different process conditions. The key assumptions for the different studies are summarized in Table 3 including the reference parameterization of the considered shaft furnace process in this study.

The analysis of Table 3 reveals the presence of a multitude of varying inlet conditions (e.g. reducing agent temperature ranging from 500 to 980 °C, initial pellet temperature ranging from 25 to 800 °C and outlet conditions (e.g. top gas temperature ranging from 250 to 800 °C, pellet temperature ranging from 700 to 800 °C), alongside different heat supply methods (such as electrical, natural gas combustion, hydrogen combustion, or oxygen injection into the shaft). These factors, combined with the different scopes of the studies, result in significant variations in specific energy demands per tonne of reduced iron, ranging from 3.48 to 4.24 MWh t^{-1}. These substantial deviations can primarily be attributed to variations in scope, heat recovery efforts, electrolyzer efficiencies, and the nature of the external heat supply. It should be emphasized that all studies listed, including the present one, focus on exploring the potential of SF-HDR concepts. While they may not provide a highly precise description of the shaft furnace reactor, they are ensuring that the process is not equilibrium-limited (cf. Fig. 3). However, it becomes evident that there is a lack of integration between kinetic studies [89–92], advanced computational fluid dynamics (CFD) simulations of SF-HDR performance [93–97] under different operational conditions (e.g. residence times, temperature profiles, pressure, GOD, λ_{H_2}, pellet sizes) and sophisticated, yet manageable, reactor models for process simulation and optimization.

Melting and atomization: Iron powders in large quantities are produced by melting and subsequently atomizing the superheated melt

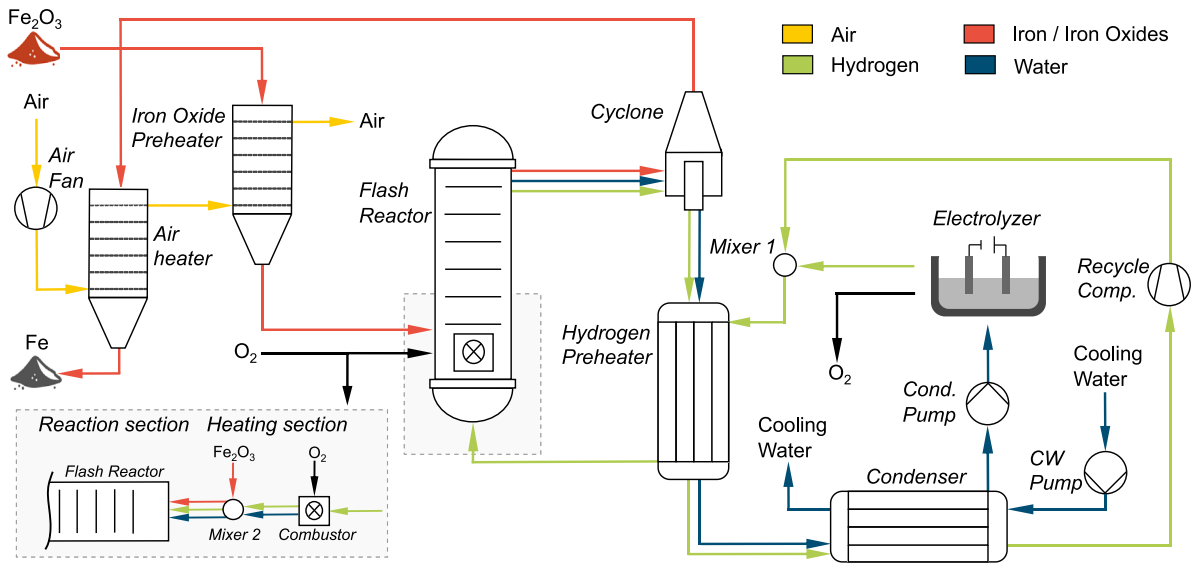

Fig. 6. Schematic of the investigated FR-HDR plant.
Source: Adapted based on [105].

with water [98]. Hot reduced iron pellets are fed directly into an electric arc furnace (EAF) [99,100], where they are heated and melted at 1600 °C along with a slag former (CaO 50 kg t_{iron}^{-1} [101]). Nevertheless, the prevailing approach in modern EAF ironmaking involves maximizing the utilization of fossil ECs, in addition to electric energy, to enable shorter tap-to-tap durations [100]. A drawback is the high energy content (sensible and chemical energy of unburned fuel) leaving the EAF referred to as off-gas [100]. However, for the EAF in this study it is assumed that 100% of the required melting energy is supplied through green electricity, eliminating the losses associated with the off gas. It is worth noting that heat losses resulting from radiation and cooling requirements for the panels account for approximately 10% of the total energy input [100]. The hot melt is then conveyed to an atomizer. Here, the liquid iron is dispersed up into a fine spray that quickly solidifies into powder [102]. The median particle size is primarily influenced by the water pressure and jet angles [103]. For the atomization process under investigation, a water to melt flow ratio of 2.5 and a water pressure of 250 bar is presumed, leading to median particle sizes on the range of 30 µm [98]. Generally, water atomization is more cost-effective than other atomization methods, such as gas atomization, due to the lower cost of the medium (water) and reduced energy use for pressurization [104]. However, the limitations of water atomization include powder purity and particle shape. The process often results in more irregular shaped particles compared to gas atomization with some oxygen content due to partial oxidation of the iron by water [104].

3.2.2. Flash reactor hydrogen direct reduction (FR-HDR)

An alternative technology with lower energy demand and capital investment requirements is the FR-HDR process developed at the University of Utah [50,59,106–108]. This innovative concept offers significant potential as it can directly utilize fine iron ore particles without any additional pre- and post-treatment, eliminating the need for pelletization and the powder production in the context of the iron-based energy cycle. The fine particle size (average particle sizes in the range of 20 µm [106] to 45 µm [108]) enables very rapid reaction rates, resulting in short residence times (in the order of seconds) compared to the longer residence times (minutes to hours) in shaft furnace or fluidized-bed reactors. Unlike other direct reduction furnaces, the flash reactor reduction technology is a high-intensity process, free from the problems associated with operating at high temperatures [107], such as particle sticking in fluidized bed reactors [72,73,109,110] or shaft furnace reactors [111–113]. The investigated FR-HDR plant is depicted in Fig. 6. The starting point is fine iron oxide powder (the outcome of the preceding oxidation process) serving as the feedstock, which undergoes preliminary heating in an iron oxide preheater. Subsequently, this preheated powder is directed into the flash reactor, where it reacts with a stream of hydrogen, resulting in the formation of iron and water, as illustrated by Eq. (2). The endothermic characteristics of the reduction reaction necessitate an auxiliary heat source, which can be generated internally by utilizing some of the reducing agent (H_2) via partial oxygen combustion, using part of the by-product oxygen from the electrolyzer. Subsequently, the reactor effluent undergoes separation in a cyclone. The hot iron, upon exiting the cyclone, undergoes cooling via an air heater, which harnesses the residual heat to pre-warm the iron oxide feed using air as a secondary medium. The heated hydrogen discharged from the cyclone is used within a regenerative heat exchanger (hydrogen preheater) to pre-warm the gaseous reactants before they enter the flash reactor. A majority of the water content in the recycle stream is removed via a condenser, and the residual hydrogen is merged with the hydrogen produced by the electrolyzer. The flash reactor is the crucial component of the process. Experimental findings [108] and numerical evidence [114] suggest that full conversion of iron oxides to iron using hydrogen at atmospheric pressure is plausible. The flash reactor is conceptualized as a sequence comprising a combustor, a heating section (adiabatic mixer), and a reaction section (adiabatic yield reactor), as shown in Fig. 6.

Furthermore, there are indications that flash-reduced iron particles exhibit a lower susceptibility to oxidation atmospheres in comparison to their conventional direct-reduced iron counterparts [115]. The higher reduction temperatures inherent in the flash reduction process yield iron powder with decreased specific surface areas [115]. This enhancement in oxidation resistance presents potential advantages for transportation, intermediate storage, and handling procedures by mitigating unwanted oxidation.

4. Release: Iron-fired power plant (IFPP)

A promising method for heat and power generation referred to as the dry cycle, involving the combustion of metal fuels, has recently been proposed [33,35,116]. In this section essential background information on the key reactions and equilibrium considerations governing iron dust air flames is provided, along with the implications of current knowledge in this field. Additionally, the potential and implications for retrofitting a CFPP into an IFPP is evaluated using a generic CFPP as the basis for subsequent assessments.

4.1. Thermodynamics of iron combustion

Among potential metal fuels such as aluminum [38] and magnesium [117,118], iron is particularly noteworthy due to its heterogeneous oxidation temperature being lower than the boiling point of iron and its oxides [33]. This distinctive characteristic theoretically prevents the formation of iron/iron oxide particles in the gas phase (i.e. the formation of nanoparticles), thereby enabling efficient post-combustion collection of the solid oxides. As a result, iron represents a highly promising candidate for the dry cycle process. The oxidation of iron and its oxides to hematite is presented below:

$$\mathrm{Fe} + \frac{3}{4}\,\mathrm{O_2} \rightarrow \frac{1}{2}\,\mathrm{Fe_2O_3}\,, \tag{8}$$

$$\mathrm{Fe_zO} + \frac{1}{4}z\,\mathrm{O_2} \rightarrow \frac{1}{2}z\,\mathrm{Fe_2O_3}\,, \tag{9}$$

$$\mathrm{Fe_3O_4} + \frac{1}{4}\,\mathrm{O_2} \rightarrow \frac{3}{2}\,\mathrm{Fe_2O_3}\,. \tag{10}$$

In the same manner as for the reduction of iron oxides, an oxygen equivalence ratio $\lambda_{\mathrm{O_2}}$ can be defined by

$$\lambda_{\mathrm{O_2}} = \frac{\text{available oxygen quantity}}{\text{stoich. required oxygen quantity}}\,,$$

$$\lambda_{\mathrm{O_2}} = \frac{N_{\mathrm{O_2}}}{0.75 \cdot N_{\mathrm{Fe}} + 0.25 \cdot N_{\mathrm{Fe_3O_4}} + 0.25z \cdot N_{\mathrm{Fe_zO}}}\ \left[\frac{\mathrm{mol}}{\mathrm{mol}}\right]. \tag{11}$$

Contrary to the combustion of coal or natural gas, simple combustion calculations for iron do not yield satisfactory theoretical adiabatic combustion temperatures. This is attributed to the fact that the stable phases of iron and its oxides are heavily dependent on both the temperature and the available oxygen, as depicted in Fig. 7, which presents the Fe-O phase diagram for a partial oxygen pressure of 0.21 bar. Further insights can be gained by analyzing the diagram together with the adiabatic equilibrium combustion temperatures, represented by the colored lines in Fig. 7. In the figure, an air temperature of 25 °C (blue line) and 400 °C (red line) are distinguished. Interestingly, the highest temperatures occur during fuel-rich conditions, i.e. for $\lambda_{\mathrm{O_2}} = 0.76$ and $\lambda_{\mathrm{O_2}} = 0.73$ at air temperatures of 25 °C and 400 °C, respectively. Fig. 7 also indicates that the combustion of iron in air can involve phase changes, such that the initially solid iron particles can burn either in the solid phase or as liquid droplets. These characteristics entail challenges for process control, such as the formation and emission of unwanted nanoparticles, which are to be minimized. From a technological perspective, it has to be further shown whether suitable flow control can prevent adhesion of iron/iron oxides to the combustor walls or heat exchanger surfaces, which is to be avoided to sustain a stable operation of the process. Otherwise, it could become necessary to maintain combustion temperatures below the melting points of iron and its oxides. However, achieving this could require very high oxygen equivalence ratios, which increase the auxiliary power demand and consequently reduces the net efficiency of the power plant. A promising alternative solution to this challenge is to decrease the oxygen concentration of the oxidation atmosphere, which can be readily accomplished through flue gas recirculation (FGR). The dashed lines in the diagram represent the adiabatic combustion temperatures for an oxygen concentration of 10%. Under these process conditions, the theoretical combustion temperature can be kept below the melting points with moderate air equivalent ratios. The impact of these process conditions on power plant operation will be further explored later.

Although the rapid heating and cooling processes during the combustion of iron particles may not adhere to equilibrium conditions, the Fe–O binary phase diagram remains a useful reference for anticipating potential phase changes. However, real-world combustion applications may significantly deviate from these theoretical equilibrium predictions, which is subsequently further outlined.

4.2. Iron dust flames

There exists a considerable amount of fundamental research on metal flames, including iron, as reviewed by Bergthorson et al. [33]

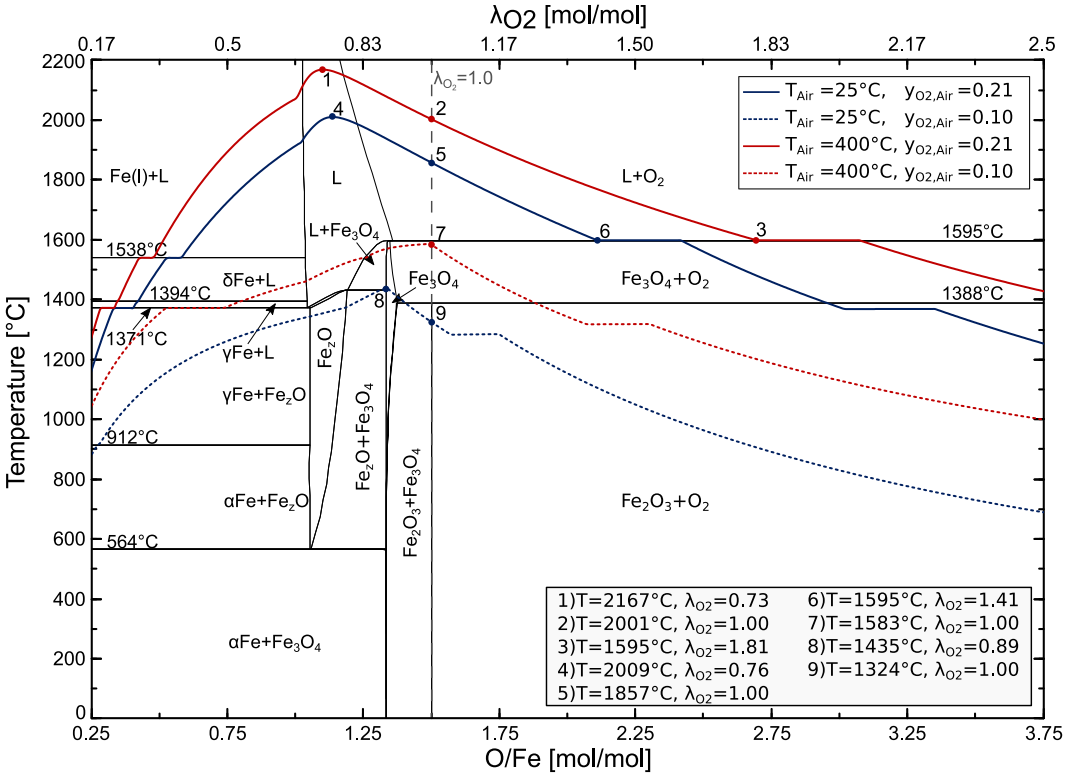

Fig. 7. Phase Diagram of the Fe–O–System at an oxygen partial pressure of 0.21 bar. The black lines distinguish regions containing different species, while the colored lines represent the theoretical adiabatic combustion temperatures based on thermodynamic equilibrium for different air temperatures and oxygen concentration. The phase of molten iron oxides consisting of Fe_zO and Fe_2O_3 is denoted as L. The diagram and the adiabatic equilibrium temperature are based on FactSage 8.2 [57], utilizing the FactPS and FTOxid databases.

and more recently by Goroshin et al. [119]. Besides the pioneering research on metal fuels carried out at McGill University in Canada, recent research programs on the subject emerged in the Netherlands, Germany, Sweden, France, USA, and China. Although progress has been made with respect to the understanding of the combustion of iron and other metals, many scientific questions have yet to be answered. In the following, the most important application-relevant aspects of iron dust flames are summarized.

While other solid fuels, such as coal and biomass, release volatile matter which promotes flame stabilization, iron burns in a non-volatile manner, i.e. chemical reactions and the associated heat release occur at the single particle scale. Iron particles are therefore sometimes referred to as micro-reactors or flame-in-a-flame [119]. There exist significant differences between such non-volatile iron dust flames and the conventional volatile solid fuel flames or gaseous flames as pointed out by Goroshin et al. [119]: The iron particles (or droplets) can significantly exceed the gas temperature. Fuel concentration and temperature profiles differ since the fuel (i.e. iron) does not diffuse, and the flame structure becomes distorted due to thermal inertia and phase transitions of the iron. In consequence, the flame's speed and temperature show a much weaker response to the fuel-oxygen equivalence ratio as compared to gas flames. Compared to conventional hydrocarbon fuels, flame speeds of iron dust flames are rather low, such that some authors used additional gaseous fuel (e.g. CH_4) to achieve flame stabilization [120]. It has further been shown that smaller particles (few microns) promote flame speed and also enhance flame stabilization [119]. Generally, due to the high densities of iron and its oxides, iron microparticles need to be significantly smaller than coal or lignite particles to achieve similar sinking velocities ($\mathcal{O}(5-40\,\mu m)$ for iron, compared to $\mathcal{O}(200\,\mu m)$ for coal [42]). In terms of emissions, the combustion of iron powder does not produce greenhouse gases and, despite the high temperatures, showed only minor NO_x formation [36,41]. As mentioned before, one of the main issues are nanoparticle emissions [121–123], which originate from the evaporation of hot iron droplets during high temperature oxidation. Experiments have shown that nanoparticle formation can effectively be suppressed by lowering combustion temperatures, e.g. through lowered oxygen concentrations [124–126] (achievable for instance by FGR).

In the past, iron dust flames have been established experimentally in different configurations, such as counterflow flames [127], Bunsen flames [33,120,128], laminar lifted flames [129], or top-fired swirled tornado flames [126]. Furthermore, demonstration-scale reactors are already being operated [41]. Of the aforementioned works, the study by Baigmohammadi et al. [126] already provides relevant information for the design of industrial metal combustors. The authors have demonstrated operation of a lab-scale 5 kW top-fired combustor with iron and confirmed self-sustained operation both for freshly atomized and recycled/regenerated iron powders. Stable operation could also be shown for reduced oxygen atmospheres. Only during start-up of the combustor, electric heaters were required to reach at a suitable system temperature, but they could be switched off after this initiation phase. Varying the equivalence ratio showed an effect on the conversion efficiency (oxidation degree) of the iron particles in the study. Nevertheless, it is to be expected that the complete particle burnout becomes an optimization target at later stages and will be improved significantly as the technology matures.

4.3. Reference coal and iron-fired power plant (CFPP & IFPP)

Modern CFPPs with steam of 600 °C/620 °C and up to 300 bar achieve net efficiencies of up to 47% [130,131]. Future CFPPs with even higher steam parameters are projected to reach efficiencies above 50% [131,132]. For the ensuing analysis, a generic ultra-supercritical CFPP is assumed. The plant, schematically shown in Fig. 8, has a gross power $P_{rel,gr}$ of 800 MW. A generic bituminous coal with a lower heating value (LHV) of 30 MJ kg^{-1} is considered as fuel. The key design parameters are given in Table 4. The steam cycle is simulated using fundamental principles, whereas certain auxiliary components like flue gas desulfurization, coal milling, and fuel handling and dedusting are modeled in a simplified manner. The energy requirements for these auxiliary units are based on established literature values. The specified CFPP exhibits a

Table 4
Key design parameters for the reference CFPP.

Parameter	Value	Parameter	Value
$\dot{m}_{ms}$	561 kg s^{-1}	$\dot{m}_{coal}$	57 kg s^{-1}
T_{ms}	600 °C	$\dot{m}_{air}$	697 kg s^{-1}
p_{ms}	275 bar	$\lambda_{O_2,coal}$	1.2
$\dot{m}_{rs}$	500 kg s^{-1}	p_{cond}	0.045 bar
T_{rs}	620 °C	$T_{fg,out}$	140 °C
p_{rs}	61 bar	P_{net}	800 MW

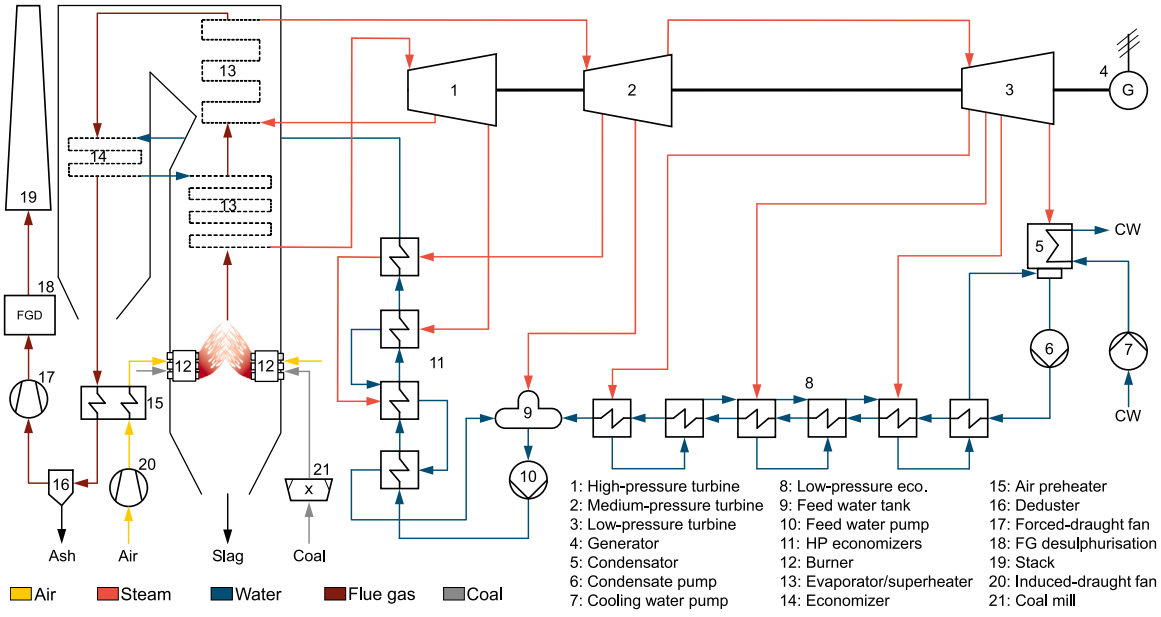

Fig. 8. Schematic diagram of the generic coal-fired power plant.

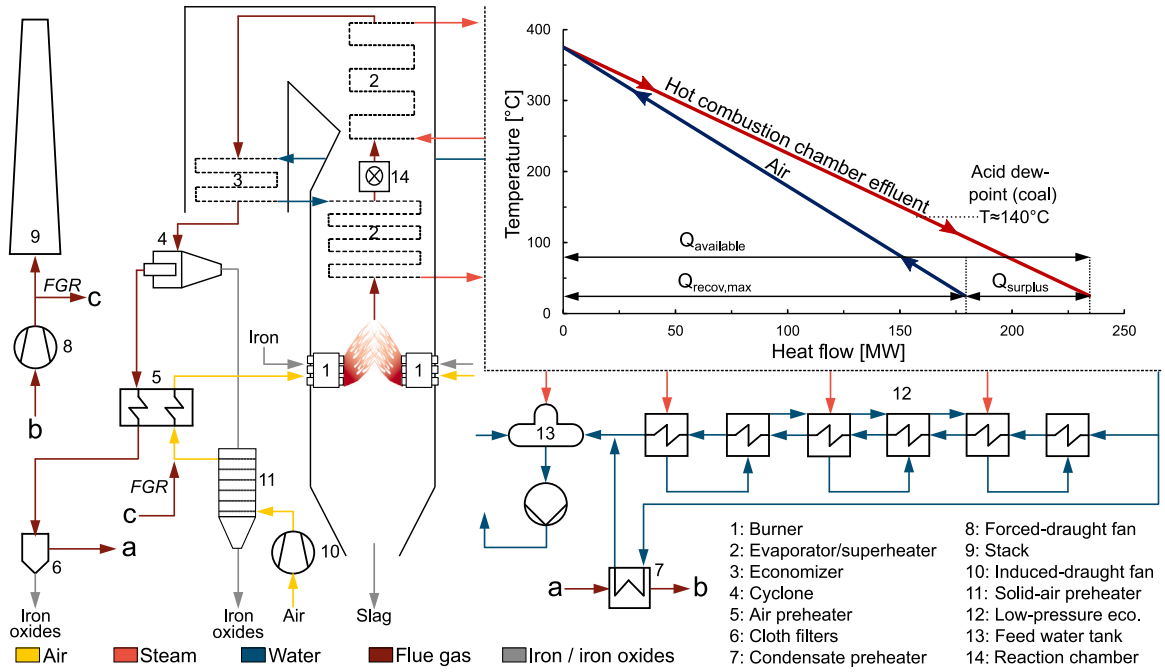

Fig. 9. Schematic diagram of the IFPP and the composite curves for the combustion chamber effluents and air (λ_{O_2} = 1.2, full oxidation to Fe_2O_3, no FGR).

net efficiency of 44.8%, with individual efficiencies of 93.9%, 51.3%, and 93.1% for the boiler, turbine/generator, and auxiliary efficiency, respectively.

Janicka et al. [42] conducted the first comprehensive case study on retrofitting an existing CFPP for operation with green iron. They utilized a highly detailed and sophisticated model of a state-of-the-art CFPP, incorporating all essential control loops and real operation conditions of the equipment. They concluded that the conversion of a CFPP to iron operation is not only feasible but likely leads to efficiency improvements, with several moderate modifications:

- Conversion of the fuel feeding system for operation with iron,
- Redesign of the solid fuel burners,
- Flue gas dedusting to reliably remove the oxidized microparticles,
- Removal of redundant components such as mills, desulfurization, and supposedly the de-NO_x system,
- Revision of the cleaning and protection systems to remove deposits from heating surfaces.

It can be assumed that most of the above measures can be solved by means of conventional mechanical engineering approaches [42]. However, further research is necessary with respect to the redesign of solid burners. Besides the stabilization of turbulent iron dust flames in general, aspects such as the influence of preheating of the iron powder or polydispersity [133] on the turbulent flame behavior needs to be understood.

The model outlined here for an IFFP (as shown in Fig. 9) has specific characteristics. While it does not consider detailed heat transfer analysis, it does have several additional features. These include a cyclone separation system for particles, a bulk-solid heat exchanger designed to recuperate sensible heat from solid reaction products, and crucially, a FGR system. The FGR system is particularly noteworthy as it can be employed to fine-tune both, reaction temperature and oxygen concentration. This adaptability allows for customization of reaction conditions to reflect the latest insights and indications concerning the combustion of iron in industrial burners. For example, it enables the reduction of nanoparticle formation by controlling oxygen concentration, and adjusting the theoretical combustion temperatures.

Furthermore, an IFPP benefits from the absence of constraints such as the sulfuric acid dew point, which typically is in the range of 140 °C [134]. This enables substantial more exploitation of the sensible heat from the reaction products compared to a CFPP. An examination of the composite curves of reaction educts and products (illustrated in the top right of Fig. 9) reveals that the available heat exceeds the energy needed to warm the cold air by a significant margin. This surplus energy is re-coupled to the process by a condensate preheater (component 7 in Fig. 9). This increases the net efficiency of the proposed IFPP. The combustion chamber is conceptualized as a dual-stage yield reactor. During the initial stage of reaction (burners), the oxidative process is constrained to yield magnetite (X_{ox} = 0.89), taking thermodynamic equilibrium considerations into account. Following the superheater/evaporator, oxidation to higher degrees can be achieved at lower temperatures in the second reaction section (reaction chamber, see Fig. 7). For the cyclone separation process, a pressure drop of Δp_{cyc} = 0.05 bar is assumed, a value estimated through initial calculations as outlined in [135]. Furthermore, it is assumed that 1% of the solid reaction product exits the combustion chamber as nanoparticles, which are then separated by cloth filters with a pressure drop of 0.02 bar. This is half the value previously considered by Janicka et al. [42], who relied exclusively on cloth filters for particle separation. Lastly, it is assumed that 0.5 wt% of the particles from the first reaction section fall as slag into the ash hopper below. The implications and impact of these assumptions are evaluated in subsequent sections of this study.

5. Transport, intermediate storage, and handling

Iron oxides and direct reduced iron (DRI), whether in briquetted or fine forms, are frequently handled using standardized protocols for bulk solids on a worldwide industrial scale. However, special precautions and considerations are required by these materials' unique characteristics to guarantee safe and efficient transportation, storage, and handling. In this section, an overview of the current best practices is presented, drawing on established experiences and standards specific to DRI.

Transport: In 2021, maritime transport of iron oxide/ores reached 1517 million tons, making up 28% of the total dry bulk shipped [136]. The International Maritime Organization (IMO), a United Nations

specialized agency, oversees the international shipment of solid bulk cargoes. According to the International Maritime Solid Bulk Cargoes (IMSBC) code [137], the main hazard with maritime transport of fine iron ores is liquefaction: Forces during transport cause the spaces between moist grains to contract, reducing friction and leading to so-called liquefaction if moisture exceeds certain levels. This can hinder maneuverability and may even cause a ship to capsize.

In 2022, a total of 25.7 million tons (22.2 in 2021) of DRI were shipped, with 15.7 million tons transported by land and 10 million tons transported by sea [87]. The reliable transportation of DRI by rail may require special containers for dusty, trickling and moisture-sensitive goods, which are being actively developed by the industry [138]. The IMSBC code [137] classifies three different forms of DRI (DRI A, B, C), where DRI C corresponds to particle sizes less than 6.35 mm, and provides recommendations for their safe handling and maritime transport. The hazards associated with DRI and its derivatives are twofold. First, it reacts with air, leading to heat generation, auto-oxidation, and incandescence. Second, the material reacts with moisture, generating explosive hydrogen air atmospheres [139]. To mitigate these risks, the IMSBC code specifically advises that DRI C cargoes (known as fines) should be transported under an inert protective blanket. Furthermore, the concentration of oxygen must be regularly monitored and controlled within safe limits. Additionally, the cargo shall be kept within the permissible moisture content at all times (0.3% limit on moisture, with the exception that the cargo shall be certified as having been aged for 30 days) [137]. According to the International Iron Metallics Association (IIMA), over 10 million tons of DRI fines have been shipped in the last decade [140]. Furthermore, the IIMA argues that the requirement for the introduction of an inert blanket is not relevant for DRI fines, since the primary hazard for fines is hydrogen evolution, and not self-heating. This hazard can be better counteracted by mechanical ventilation to prevent accumulation of hydrogen [140].

In addressing the logistics associated with the considered iron-based energy cycle, one must account for the increased mass of the oxidized iron due to the oxygen-binding during the oxidation process. Upon full oxidation of pure iron ($X_{ox} = 0$) to hematite ($X_{ox} = 1$), the mass of the resultant iron oxide increases by 43%. This substantial increment in mass must be factored in while determining the energy requirements for the return journey of the depleted EC.

The energy required for long-distance transportation E_{tra} utilizing bulk solid vessels can be normalized by the transported cargo weight and the transport distance, leading to 6–8 kWh $(1000\ \text{km}\ t_{cargo})^{-1}$. These specific fuel demands are estimated based on the data provided in [141] for Capesize and very large bulk carriers, assuming a nominal speed of 14.5 knots and the maximum continuous rating of the engine with an efficiency of 50% [142]. Presently, maritime transport is predominantly dependent on fossil fuels, specifically heavy fuel oil [136]. However, the sector is actively pursuing decarbonization [136].

Intermediate storage: DRI fines can be stored in stockyards, warehouses, or hoppers [140]. When storing DRI fines in stockyards or warehouses, proper precautions should be taken. For storage in silos or hoppers, monitoring the hydrogen concentration in the enclosed space and employing mechanical ventilation are recommended to ensure safety [140]. The storage of iron oxides generally does not require special precautions due to their stable nature. However, when residual iron fuel energy is present ($X_{ox} < 1$) within the iron oxides, further oxidation can result in energy losses and may affect the overall efficiency of the overarching cycle. In such cases, it might be advantageous to implement storage solutions that reduce exposure to environmental factors such as humidity and air.

Handling: Preventing any potential contact with water is vital when handling DRI fines to avoid adverse reactions. Regardless of the location, be it the production site, ports, or end-user's stockyard, handling procedures permit the use of standard bulk material handling equipment of various types, sizes, and capacities [140]. However, the handling and transfer process at each stage may generate some fine dust [140]. The handling of fine iron particles carries a potential explosion hazard [53,143–145], which is less severe compared to aluminum fines [53,143]. The explosion severity is reduced when small amounts of Fe_2O_3 or Fe_3O_4 [145] are presents, which might be the case due to incomplete reduction or re-oxidation due to contact with air.

The above considerations showcase that iron and iron oxide fines can be shipped, stored, and handled with standardized protocols for bulk solids on a global industrial scale. However, the degree of re-oxidation may vary depending on factors such as the handling procedure, the origin and the morphology of the material [146]. As such, it is necessary to consider and evaluate any changes in the oxidation state that occur during transport and storage for the evaluation of the iron-based energy cycle. This can be quantified with a change in the oxidation/reduction state during transport or intermediate storage $\Delta X_{ox,is}$. Furthermore, in the context of the introduced iron-based energy cycle, atomized iron powder might be transported, shipped, and handled. Unlike conventional DRI, atomized iron powder has a lower porosity and decreased reactivity. The metal powder particles are typically covered by thin oxide layers due to their exposure to air or oxygen-containing atmospheres, with layer thicknesses typically reported to be in the range of 5–7 nm for plain iron [147]. This corresponds to a negligible volume fraction of approximately 0.1% considering a sphere with a diameter of 30 µm.

When it comes to storing, transporting, and handling iron, there is a trade-off between the efforts to prevent oxidation and allowing some losses. While using hermetically-sealed containers or bags can effectively prevent oxidation (high effort), exposure to humidity and oxygen (low effort) in the atmosphere may result in some oxidation and consequently depletion of the energy carrier. The impact of potential re-oxidation on the cycle efficiency is later evaluated.

6. Performance evaluation criteria

The evaluation of the previously discussed process models, which investigate the oxidation process in IFPPs for carbon-free electricity generation, as well as the thermochemical reduction process in the context of SF-HDR and FR-HDR plants, is performed based on their energetic efficiencies. The subsequent section defines performance metrics for the individual sub-processes, as well as the comprehensive interconnected system of the aforementioned iron-based energy cycle. The referenced variables are provided in the schematic of the investigated iron-based energy cycle in Fig. 1.

6.1. Storage: Hydrogen direct reduction of iron oxides

The net efficiency of the reduction concepts as outlined earlier is defined by the increase in iron fuel energy $E_{Fe_xO_y}$ ($E_{Fe_xO_y} = m_{Fe_xO_y} \cdot HV_{Fe_xO_y}$) within the iron (oxides) during the reduction process (taking into account the starting and attained reduction degree), relative to the total required energy $E_{sto,tot}$ of the process:

$$\eta_{sto,net} = \frac{E_{Fe_xO_y\,sto,out} - E_{Fe_xO_y\,sto,in}}{E_{sto,tot}}. \tag{12}$$

To pinpoint the sources of efficiency loss, the net efficiency is divided into the reduction efficiency $\eta_{sto,red}$, which considers the energy demand of hydrogen production required for the reduction in relation to the increase in chemical energy stored in the iron fuel, and a peripheral efficiency $\eta_{sto,per}$, which accounts for all necessary peripheral energy requirements in relation to the total energy demand of the HDR plants:

$$\eta_{sto,net} = \eta_{sto,red} \cdot \eta_{sto,per}, \tag{13}$$

$$\eta_{sto,red} = \frac{E_{Fe_xO_y\,sto,out} - E_{Fe_xO_y\,sto,in}}{E_{sto,red}}, \tag{14}$$

$$\eta_{\mathrm{sto,per}} = \frac{E_{\mathrm{sto,red}}}{E_{\mathrm{sto,tot}}} = 1 - \alpha_{\mathrm{red,heat}} - \alpha_{\mathrm{red,aux}} - \alpha_{\mathrm{pel}} - \alpha_{\mathrm{EAF}} - \alpha_{\mathrm{ato}} \,. \tag{15}$$

The peripheral efficiency given in Eq. (15) can be represented by the relative energy requirements for providing the process heat for the reduction $\alpha_{\mathrm{red,heat}}$, auxiliary energy inputs for plant balance $\alpha_{\mathrm{red,aux}}$ and, if applicable, additional energy requirements for the pelletization α_{pel}, the EAF α_{EAF}, and the atomizer α_{ato}.

6.2. Release: Iron-fired power plant

The net efficiency of a CFPP is determined by the net electrical energy $E_{\mathrm{rel,net}}$ (gross electrical energy $E_{\mathrm{rel,gr}}$ minus the necessary auxiliary electrical energy $E_{\mathrm{rel,aux}}$) divided by the product of the fuel mass m_{f} and the fuel's lower heating value LHV_{f} [134]:

$$\eta_{\mathrm{rel,net}} = \frac{E_{\mathrm{rel,net}}}{m_{\mathrm{f}} \cdot LHV_{\mathrm{f}}} \,. \tag{16}$$

In the same manner as for the storage process, the net efficiency is separated into individual efficiencies such as the boiler efficiency $\eta_{\mathrm{rel,b}}$, the turbine/generator efficiency $\eta_{\mathrm{rel,tg}}$, and the auxiliary power efficiency $\eta_{\mathrm{rel,aux}}$ (the necessary electrical auxiliary power):

$$\eta_{\mathrm{rel,net}} = \eta_{\mathrm{rel,b}} \cdot \eta_{\mathrm{rel,tg}} \cdot \eta_{\mathrm{rel,aux}} \,. \tag{17}$$

The energy from the fuel is not completely transferred to the steam due to various losses, such as losses from unburned combustibles β_{u}, losses from the sensible heat of the slag β_{sl}, flue gas losses β_{fg}, and heat losses from the steam generator to the environment β_{env}:

$$\eta_{\mathrm{rel,b}} = \frac{\sum m_{\mathrm{s},j} \cdot \Delta h_j}{m_{\mathrm{f}} \cdot LHV_{\mathrm{f}}} = 1 - \beta_{\mathrm{fg}} - \beta_{\mathrm{env}} - \beta_{\mathrm{u}} - \beta_{\mathrm{sl}} \,. \tag{18}$$

The turbine/generator efficiency is the ratio of the gross electrical output (which includes mechanical losses of the turbine shaft and generator efficiency) to the supplied steam energy:

$$\eta_{\mathrm{rel,tg}} = \frac{E_{\mathrm{rel,gr}}}{\sum m_{\mathrm{s},j} \cdot \Delta h_j} \,. \tag{19}$$

The auxiliary efficiency represents the energy requirements of the auxiliary units relative to the gross electrical energy, and it can be expressed as unit-specific losses γ_i:

$$\eta_{\mathrm{rel,aux}} = \frac{E_{\mathrm{rel,ne}}}{E_{\mathrm{rel,gr}}} = 1 - \sum_i \gamma_i \,. \tag{20}$$

Common boiler losses and auxiliary energy requirements are specified in Tables 5 and 6, respectively, which are in line with the parameterization performed.

Table 5
Typical relative boiler losses based on fuel energy for CFPPs.

Reference	Spliethoff [134]	Strauss [148]	This study
Flue gas losses β_{fg}	3.8–5.3%	6–10%	5.3%
Boiler radiation β_{env}	0.25–0.3%	0.2–1%	0.3%
Unburned material β_{u}	0.3–0.5%	0.5–1.5%	0.5%
Slag β_{sl}	0.04%	0.2%	0.1%
Boiler efficiency $\eta_{\mathrm{rel,b}}$	93.9–95.6%	87.3–93.1%	93.8%

Table 6
Typical relative auxiliary energy demand based on the gross generator power.

Reference	Spliethoff [134]	Strauss [148]	This study
Pumps γ_{pump}	3.3–4.5%	3.8%	3.4%
Fans γ_{fan}	1.3–2%	1.6%	1.4%
Mills γ_{mill}	0.4%	0.2%	0.3%
Fuel handling γ_{fh}	0.3%	NA	0.3%
FGD γ_{fgd}	0.8–2%	1%	1.5%
Aux. efficiency $\eta_{\mathrm{rel,aux}}$	90.8–93.9%	93.4%	93.1%

The aforementioned performance evaluation criteria can also be applied to a carbon-free IFPP. However, unlike in conventional CFPPs, where unburned combustibles contribute significantly to the boiler losses (cf. Table 5), the circularity of the iron fuel eliminates such losses. Instead, partially oxidized iron powder ($X_{\mathrm{ox}} < 1$) is directed to subsequent stages of the process, such as intermediate storage and transport. The remaining iron fuel energy within the ash, which descends from the boiler to the ash hopper, is regarded as boiler losses due to unburned combustibles (β_{u}). Similar to the storage process, the reduction in iron fuel energy during oxidation, relative to the net electrical energy of the power plant, can be used to determine the aggregated release efficiency, given by:

$$\eta_{\mathrm{rel,net}} = \frac{E_{\mathrm{rel,net}}}{E_{\mathrm{Fe_xO_y\,rel,in}} - E_{\mathrm{Fe_xO_y\,rel,out}}} \,. \tag{21}$$

Due to the introduced condensate preheater, the steam energy ($\sum m_{\mathrm{s},j} \cdot \Delta h_j$) within Eqs. (18) and (19) is adapted to cover the additional supplied heat to the steam cycle. Furthermore, there are no losses associated with mills and flue-gas desulfurization (FGD) since the iron fuel possesses the appropriate morphology and does not contain sulfur. Additionally, losses due to flue gas denitrification are not considered, as recent studies have shown only minor NO_x formation [36,41].

6.3. Overarching iron-based energy cycle

The efficiency assessment of the described power-to-power cycle requires a comprehensive balance of all energy inputs and outputs, which include storage and transport, as well as potential losses throughout the cycle. These losses stem from the storage or release process as well as from undesired oxidation during intermediate storage or from potential material losses. The functional unit of the cycle is the electrical energy released during the release step. In line with the proposed iron-based energy cycle (cf. Fig. 1) the cycle efficiency η_{cyc} can be approximated from the efficiencies of the chained sub-processes according to:

$$\eta_{\mathrm{cyc}} = \frac{E_{\mathrm{cyc,net}}}{\sum_j E_{\mathrm{cyc,in},j}} \approx \eta_{\mathrm{sto}} \cdot \eta_{\mathrm{is}} \cdot \eta_{\mathrm{tra}} \cdot \eta_{\mathrm{mat}} \cdot \eta_{\mathrm{rel}} \cdot \eta_{\mathrm{rep}} \,. \tag{22}$$

The efficiencies related to storage (η_{sto}) and release (η_{rel}) correspond to Eqs. (12) and (17), respectively. Additionally, the transport efficiency η_{tra} represents the ratio of the required auxiliary energy for transport $E_{\mathrm{tra},i}$ (considering both directions, indicated by index i) to the total energy supplied to the cycle ($\sum_j E_{\mathrm{cyc,in},j}$):

$$\eta_{\mathrm{tra}} = 1 - \frac{E_{\mathrm{tra},1} + E_{\mathrm{tra},2}}{\sum_j E_{\mathrm{cyc,in},j}} \,. \tag{23}$$

The intermediate storage efficiency η_{is} accommodates potential losses during intermediate storage (partial oxidation) $E_{\mathrm{is,i}}$ at both sites (exporting and importing, denoted by index i) in relation to the available chemical energy at each site:

$$\eta_{\mathrm{is,i}} = 1 - \frac{E_{\mathrm{is,i}}}{E_{\mathrm{Fe_xO_y,i}}} \,. \tag{24}$$

The material efficiency η_{mat} accounts for potential material losses during the transport from the storage location to the importing site due to inadequate handling (e.g. residual material in the vessels):

$$\eta_{\mathrm{mat}} = \frac{E_{\mathrm{Fe_xO_y\,rel,in}}}{E_{\mathrm{Fe_xO_y\,tra,1,out}}} \,. \tag{25}$$

Finally, the assumption is made that material losses, either due to improper handling or the formation of nanoparticles, need to be replenished. This is accounted for by the reproduction efficiency η_{rep}, which covers the energy requirements for preparing iron oxides E_{rep} to be reintroduced into the cycle to compensate potential material losses:

$$\eta_{\mathrm{rep}} = 1 - \frac{E_{\mathrm{rep}}}{\sum_j E_{\mathrm{cyc,in},j}} \,. \tag{26}$$

The introduced interlinking sub-processes efficiencies can be summarized to a miscellaneous η_{misc} efficiency:

$$\eta_{misc} = \eta_{tra} \cdot \eta_{is} \cdot \eta_{mat} \cdot \eta_{rep}\,. \tag{27}$$

The efficiencies introduced above serve as evaluation criteria in the subsequent assessments. All further results are obtained with the software EBSILON®*Professional* [55], utilizing the thermodynamic reference data provided in Ref. [56].

6.4. Morris sensitivity analysis

To understand how target variables are influenced by input variables effective modeling approaches integrate uncertainty/sensitivity analyses. Sensitivity analyses methods can be categorized into local and global approaches. The local methods, sometimes referred to as "one factor at a time", are typically used to modify one input variable sequentially from a baseline configuration. However, these local methods contrast with global methods, which require substantially more model evaluations, the volume of which escalates with the increase in the number of considered inputs. A particularly effective screening sensitivity method, balancing precision and efficiency, was introduced by Morris [149] and enhanced by Campolongo et al. [150]. It overcomes the limitation to one fixed baseline configuration by executing a set number of randomized local alterations at varying points combined with statistical operations. The method is hereafter summarized based on Refs. [149,150].

The Morris sensitivity analysis focuses on creating R trajectory designs to calculating elementary effects $EE_{i,j}$ associated with the j^{th} input factor. By performing statistical operations, a global approximation is obtained. It is organized by the following main steps:

1. **Input scaling and discretization**: All input variables are normalized to have a similar scale. This can be achieved, for instance, by linear scaling. The k-dimensional space (k input variables) is transformed in a k-dimensional ω-level grid (ω-levels for each input variable). The total number of required simulations is $(k+1)R$.
2. **Trajectory design**: A trajectory comprises points, where each subsequent point differs from its predecessor by the fixed step size $\phi = \frac{1}{(\omega-1)}$ in only one input variable. Out of M random generated trajectories, R trajectories are selected based on maximizing their dispersion in the input space in line with the approach proposed by Campolongo et al. [150].
3. **Computing elementary effects**: For every input variable j (from 1 to k), the elementary effect, denoted as $EE_{i,j}$ ($i = 1,\dots,R$, $j = 1,\dots,k$), is computed. This calculation involves taking the difference between the function value at two points differing by ϕ in the j^{th} input variable and dividing it by ϕ:

$$EE_{i,j} = \frac{f(x_1,\dots,x_j+\Delta,\dots,x_k) - f(x_1,\dots,x_j,\dots,x_k)}{\phi}\,. \tag{28}$$

4. **Moments of elementary effects**: For each input variable, the moments (i.e. mean $\mu_j^\star$ and standard deviation σ_j) of the elementary effects distribution are calculated:

$$\mu_j^\star = \sum_{i=1}^{R} \left|\frac{EE_{i,j}}{R}\right|, \tag{29}$$

$$\sigma_j = \sqrt{\frac{1}{R}\sum_{i=1}^{R}\left(EE_{i,j} - \sum_{i=1}^{R}\frac{EE_{i,j}}{R}\right)^2}\,. \tag{30}$$

Using the values of $\mu_j^\star$ and σ_j, all input parameters are categorized into three distinct groups: those with prominent linear effects without interactions (large $\mu_j^\star$, low σ_j), those displaying significant nonlinear or interaction effects (high $\mu_j^\star$, high σ_j), and those with negligible effects (small $\mu_j^\star$). Additionally, the absolute values for the elementary effects and the mean using the real parameter intervals without input scaling are determined, which can support the interpretation.

The introduced Morris sensitivity analysis will be applied to the sub-processes and the overarching cycle assessments. For all assessments, $R = 20$ trajectories out of $M = 1000$ randomized generated trajectories are selected and 4-levels for each input ($\omega = 4$, linear scaling between 0 and 1) are considered.

7. Assessment and discussion

In this section, the energetic performance based on the metrics (Section 6) of the introduced sub-processes (i.e. Storage: Section 3, Release: Section 4) and the overarching cycle including transport and intermediate Storage (Section 5) are provided and discussed. Additionally, local and Morris sensitivities of selected process parameters are determined to identify the significant operation conditions and assumptions.

7.1. Storage: Hydrogen direct reduction of iron oxides

General technological assumptions utilized for both green reduction plants (SF-HDR in Fig. 10 and FR-HDR in Fig. 11) are summarized in Table 7. Further process specific assumptions and the results are outlined in the two following sections.

7.1.1. Shaft furnace hydrogen direct reduction

Based on the assumptions outlined in Section 3.2.1 and Table 7, the net storage efficiency of the presented SF-HDR plant, including its essential peripherals, is determined as 57.3% for the specified reference case. An comparison with existing literature (cf. Table 3) reveals that the specific total energy demand for the reference case at 3.58 MWh/t, falls within the range reported for direct shaft furnace reduction plants, between 3.48 MWh/t and 4.24 MWh/t [44,45,47,88]. However, this study takes into account additional peripherals (i.e. atomizer, pelletizer), which are not considered in the previous studies. The supplementary energy demand for the atomizer is rather small, but the energy required for pelletization is notable, especially due to the process's reliance on hydrogen firing. Nonetheless, the overall impact of pelletization is mitigated by directly coupling the pelletization process with the shaft furnace, allowing the introduction of hot pellets into the furnace.

Table 8 presents the results based on the defined performance criteria. The storage reduction efficiency is 79.5%, exceeding the electrolyzer efficiency of 70%. This superior performance can be attributed to the additional heat requirements arising from the endothermic nature of the reduction reactions. The net storage efficiency, however, is compromised by a slightly lower peripheral storage efficiency of 72.1%. A significant origin of this lower efficiency is due to the energy demand for heating, accounting for approximately 5.5%. The energy required for necessary pre- and post-processing for particle size adjustment also plays a considerable role. Pelletization consumes 12.9% of the total energy demand, while the downstream EAF melting process utilizes 8.5% of the total energy. Lastly, the final step – water atomization of the hot melt to produce fine iron powder – has a minor energy demand, with the atomizer pump contributing roughly 1%.

To identify critical process conditions and assumptions, a local sensitivity analysis is conducted using the reference case as a benchmark, and the broader Morris sensitivities with respect to the net storage efficiency are determined. The local analysis, including the associated parameters and their respective intervals, is depicted in a Tornado plot on the left side of Fig. 10. Within the figure, the considered intervals including the reference case are provided for each parameter next to the bars. The results of the Morris sensitivity analysis are depicted on the right side of Fig. 10 in the form of a scatter plot. Alongside the individual data points, the absolute values of the mean of the elementary effects are also provided, aiding in a more nuanced interpretation.

Table 7
General technological assumptions for the reduction plants.

Component	Parameter	Value	Reference or comment
Pumps	Isentropic efficiency η_{isn}	75%	[151]
Compressors	Isentropic efficiency η_{isn}	80%	[151,152]
Condenser	Approach temperature ΔT	10 K	[153]
Heat exchangers	Effectiveness ϵ_{HEX}	95%	[154]
Heat exchangers	Relative heat loss $Q_{rel,loss}$ [a]	2.5%	[155]
Heat exchangers	Pressure drop Δp_{HEX}	0.1 bar	[156]
Reactor	Reduction degree in $X_{red,in}$	0	100% Fe_2O_3
Reactor	Reduction degree out $X_{red,out}$	1	100% Fe
Reactor	Relative heat loss $Q_{rel,loss}$ [a,b]	2.5%	[107]
Electrolyzer	System efficiency η_{LHV}	70%	[157]
Electric motors	Efficiency η_{mot}	95%	[153]

[a] Heat loss relative to theoretical transferred heat without losses.
[b] Allocated to heater/burner upstream the reactor.

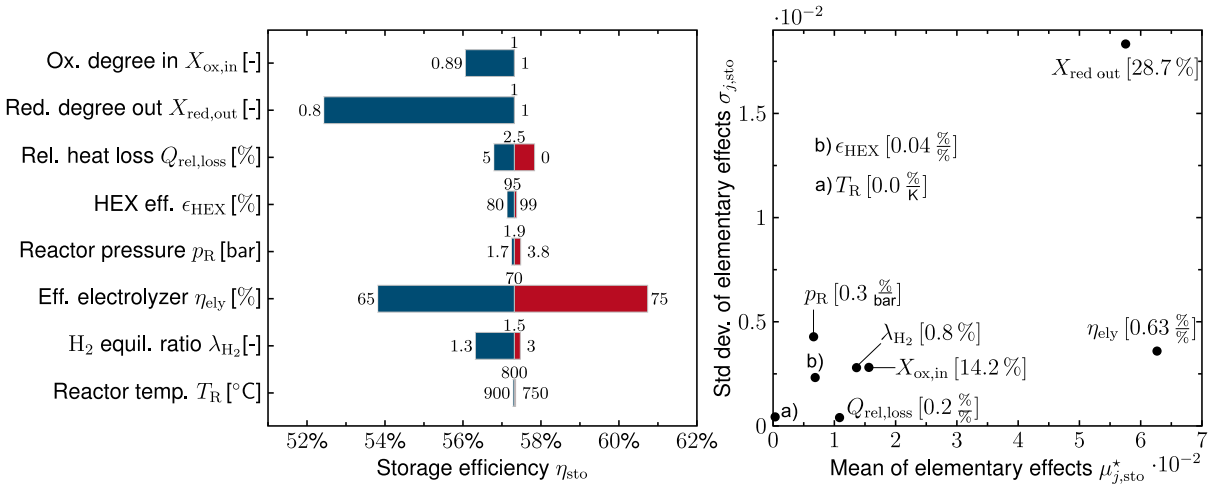

Fig. 10. Tornado plot (left) and Morris sensitivities (right) of selected parameters on the net storage efficiency for the SF-HDR plant. The considered parameter intervals are given within the Tornado plot. The values next to data points in the right graph correspond to the absolute values of the mean of the elementary effects.

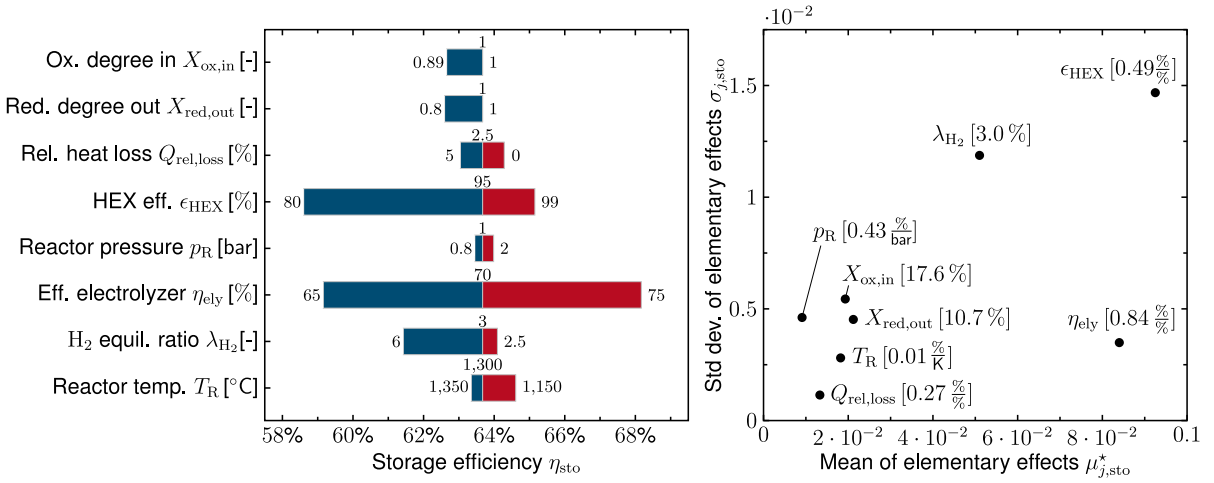

Fig. 11. Tornado plot (left) and Morris sensitivities (right) of selected parameters on the net storage efficiency for the FR-HDR plant. The considered parameter intervals are given within the Tornado plot. The values next to data points in the right graph correspond to the absolute values of the mean of the elementary effects.

Comparing these methodologies provides a holistic insight into the system's sensitivities.

As illustrated in the Tornado plot, the oxidation degree at the inlet ($X_{ox,in}$) indicates a decline in the net storage efficiency by 1.3 percentage points when magnetite ($X_{ox,in}$ = 0.89) is used as feedstock instead of hematite ($X_{ox,in}$ = 1.0). This finding is consistent with the Morris analysis, which shows moderate mean elementary effect with an absolute value of 14.2% (see value in brackets). This implies that for every 0.1 change in the oxidation degree, there is an average decrease in the net storage efficiency of 1.42 percentage points. Additionally, the mean oxidation degree at the inlet has a minimal standard deviation, indicating minimal non-linearities and a limited influence from interactions with other input parameters. The importance of the achieved reduction degree ($X_{red,out}$) is evident in both analyses. While the Tornado plot shows a decrease in the net efficiency by 5 percentage points, the Morris analysis reinforced its significance with a pronounced absolute

Table 8
Results for the SF-HDR and FR-HDR plants with respect to the defined reference case.

Performance criteria	Shaft furnace	Flash reactor
Reduction efficiency $\eta_{sto,red}$	79.5%	79.5%
Peripheral efficiency $\eta_{sto,per}$	72.1%	80.1%
Relative energy requirements		
Heat requirements $\alpha_{red,heat}$	5.5%	19.0%
Plant balance $\alpha_{red,aux}$	0.5%	1%
Pelletization α_{pel}	12.9%	0%
Electric arc furnace α_{EAF}	8.5%	0%
Atomization α_{ato}	0.7%	0%
Net storage efficiency $\eta_{sto,net}$	57.3%	63.7%

mean elementary effect of 28.7% and the highest standard deviation, indicating by far the most interactions or nonlinearities associated with the achieved reduction degree. This is primarily a consequence of the significant peripheral thermal energy demand of the process, which is further underscored by the sensitivities related to the relative heat loss of the equipment $Q_{rel,loss}$, and the effectiveness for the heat exchangers ϵ_{Hex}. The system's response to the operation pressure (p_R), indicates a moderate to small sensitivity. The electrolyzer efficiency (η_{ely}) emerges as a significant parameter in the Tornado plot (±3.5 percentage points), showing significant variation in the storage efficiency. This observation is supported by the Morris analysis, which quantified the highest mean effect with an absolute value of 0.63 %/%, suggesting its consistent influence across different operation points (trajectories). The sensitivity in relation to the hydrogen equivalence ratio λ_{H_2} is moderate. Lastly, the reactor temperature (T_R) displays stable behavior in the Tornado plot and this is supported by the Morris sensitivity analysis. This low sensitivity to temperature variations of the shaft furnace is attributed to the direct integration between the shaft furnace and the EAF.

While the visual representation from the Tornado diagram illustrates the absolute impact for a unidimensional change from the reference case, the Morris analysis quantitatively refines these findings by highlighting the central role of the electrolyzer efficiency and the achieved reduction degree independent of the defined reference parameterization.

In the proposed shaft furnace process, the sub-processes are interconnected, enabling the exploitation of the latent heat of intermediates. Disconnection of these processes results in a net storage efficiency reduction by approximately 6.2 percentage points. This reduction is split into 3.7% for the decoupling of the pelletizer and 2.5% for the decoupling of the EAF, underscoring the critical role of these interconnections in maintaining high net storage efficiencies. The later could be advantageous with respect to transport (transporting DRI pellets instead of DRI powder), but comes with the provided efficiency penalty.

7.1.2. Flash reactor hydrogen direct reduction

As pointed out in Section 3.1, the co-current flash reactor setup requires higher hydrogen equivalence ratios to circumvent thermodynamic limitations in the conversion of iron oxides to iron. This is addressed by employing a hydrogen equivalence ratio λ_{H_2} of 3. The reaction of hydrogen with oxygen, i.e. oxyfuel combustion, provides the heat needed to reach a defined temperature of 1300 °C at the reactor inlet, which is within the recommended range of 1150 - 1350 °C [106]. The internal oxyfuel combustion results in a gas oxidation degree of 10%, a factor considered in the chosen hydrogen equivalence ratio λ_{H_2} for the flash reactor (cf. Fig. 4).

For the defined reference case, the calculated net storage efficiency is 63.7%, with the partial efficiencies detailed in Table 8. The storage reduction efficiency, quantifying the increase in chemical energy stored within the iron in relation to the required hydrogen, is consistent in both scenarios, since the same reduction degrees at the inlet and outlet are assumed. The alignment of particle sizes in the storage and release steps removes the need for additional processes for particle size adjustments, leading to an 8 percentage points higher peripheral storage efficiency compared to shaft furnace reduction, thereby giving an energetic advantage to the flash reduction plant. On the other hand, the relative heating demand is notably higher (i.e. 19%), due to the increased temperatures, hydrogen equivalence ratio, and considered oxyfuel combustion.

In a manner similar to the previous evaluation of the shaft furnace, a sensitivity analysis is conducted, and the results are illustrated in Fig. 11. For a reliable comparison, the same trajectories for the SF-HDR and the FR-HDR plant assessment are used within the Morris sensitivity analysis.

The FR-HDR and SF-HDR plants, while bearing similarities, display unique sensitivities, as detailed below. For the oxidation degree at the inlet ($X_{ox,in}$), the flash reactor's analysis reveals a sensitivity similar to that of the shaft furnace reduction plant. Although the SF-HDR plant did not exhibit a notable sensitivity concerning reactor temperature, the flash reactor demonstrated a moderate sensitivity, spanning a range of 1.3 percentage points in the Tornado plot. This observation is further confirmed in the Morris plot, suggesting a moderate influence with an absolute mean elementary effect of 0.01 %/K. Conversely, the achieved reduction degree ($X_{red,out}$) ranked second most influential for the SF-HDR plant, while its impact on the FR-HDR is moderate to low, mainly due to the absence of peripheral process requirements. Beyond the reduction degree, the electrolyzer efficiency (η_{ely}) in the SF-HDR plant emerged as the most significant parameter. This is even more pronounced in the FR-HDR due to the electrolyzer's larger contribution to total energy demand, with an absolute mean elementary effect of 0.84 %/%. Another distinguishing factor between the two systems is the heat exchanger effectiveness (ϵ_{HEX}). In the FR-HDR plant, this parameter displayed the most substantial mean effect of 0.4 %/% and the highest standard deviation in the Morris analysis, underscoring its crucial role for the storage efficiency. This suggests that, relative to the SF-HDR plant, heat recovery measures are more crucial for the FR-HDR plant due to its elevated operational temperature and the absence of downstream sub-processes benefiting from increased intermediate temperatures. If the sensible heat from the iron (oxides) cannot be recovered, the net storage efficiency drops by 5.5 percentage points for the defined reference case, almost diminishing the energetic advantage of the FR-HDR plant. Similarly, the hydrogen equivalence ratio (λ_{H_2}) in the FR-HDR plant exhibited markedly higher sensitivities, with nonlinearities highlighted by an increased standard deviation, in contrast to the SF-HDR plant.

In the section presented, the two HDR plants introduced were evaluated, with FR-HDR outperforming SF-HDR. Further improvements in net storage efficiency could be achieved by utilizing the waste heat of the electrolyzer for applications such as district heating including heat pumps [158], or by incorporating an organic Rankine cycle to provide electrical energy for the system [159], thereby reducing the net demand. Recent advances in water electrolysis technologies, specifically the development of high-performance capillary-fed electrolysis cells [160], have shown promise for further efficiency gains, from which the investigated HDR plants could benefit. Subsequently, the described IFPP is assessed before the interactions of the sub-processes are evaluated within the overarching iron-based energy cycle in Section 7.3.

7.2. Release: Iron-fired power plants (ifpp)

The starting point for the assessments conducted in this section are four different scenarios for the IFPP introduced in Section 4, which are summarized in Table 9. For the reference case, full oxidation of pure iron to hematite without any restrictions is assumed. Scenario 2, termed "limited oxidation", postulates that the provided iron fuel is pre-oxidized, and the maximum achievable oxidation level is constrained by the formation of magnetite. Scenario 3, named "temperature control by λ_{O_2}", aims to keep the theoretical combustion temperature slightly below the melting point of magnetite by altering

Table 9
Assumptions for the four different IFPP operation scenarios.

Parameter	Reference	Limited oxidation	Temp. CTRL λ_{O_2}	Temp. CTRL FGR
Oxidation degree at inlet $X_{ox,in}$	0.0	0.05	0.0	0.0
Oxidation degree at outlet $X_{ox,out}$	1.0	0.89[a]	1.0	1.0
Theoretical combustion temperature T_{comb}	$f(\lambda_{O_2})$	$f(\lambda_{O_2})$	1590°C[b]	1590°C[b]

[a] Corresponds to partial oxidation up to Fe_3O_4.
[b] Slightly below the melting point of magnetite.

Table 10
Results for the reference CFPP and the introduced IFPP scenarios. The gross electric power for all cases is 800 MW. Minor discrepancies observed within the table can be attributed to rounding errors.

Parameter and	CFPP	Iron-fired power plant (IFPP)			
performance criteria	Reference	Reference	Limited oxidation	Temp. CTRL λ_{O_2}	Temp. CTRL FGR
Fuel mass flow $\dot{m}_f$ [kg/s]	55	220	264	222	221
Air mass flow $\dot{m}_{air}$ [kg/s]	677	494	551	808	453
FGR mass flow $\dot{m}_{FGR}$ [kg/s]	0	0	0	0	346
Oxygen equivalence ratio λ_{O_2} [−]	1.2	1.2	1.2	1.95	1.2
Preheated air temperature T_{air} [°C]	295	326	331	331	333
Mole fraction O_2 at burner y_{O_2} [−]	0.21	0.21	0.21	0.21	0.13
Combustion temperature T_{comb} [°C]	2034	1938	1887	1590	1590
Turbine/generator efficiency $\eta_{rel,tg}$ [%]	51.3	50.0	49.7	49.9	49.6
Boiler efficiency $\eta_{rel,b}$ [%]	93.9	98.4	98.2	98.0	99.1
Flue gas losses β_{fg} [%]	5.2	1.1	1.1	1.5	0.4
Boiler radiation losses β_{env} [%]	0.3	0.3	0.3	0.3	0.3
Unburned combustibles β_u [%]	0.5	0.05	0.2	0.05	0.05
Slag losses β_{sl} [%]	0.1	0.2	0.2	0.15	0.15
Auxiliary efficiency $\eta_{rel,aux}$ [%]	93.1	94.8	94.6	93.7	93.8
Pumps γ_{pump} [%]	3.4	3.4	3.4	3.4	3.4
Fans γ_{fan} [%]	1.4	1.5	1.7	2.56	2.47
Mills γ_{mill} [%]	0.3	0	0	0	0
Fuel handling γ_{fh} [%]	0.3	0.3	0.3	0.3	0.3
FGD γ_{fgd} [%]	1.5	0	0	0	0
Net efficiency $\eta_{rel,net}$ [%]	44.77	46.65	46.22	45.84	46.14

the air equivalence ratio. Scenario 4, termed "temperature control by FGR", parallels scenario 3 but achieves temperature control specifically through the application of the introduced FGR system.

From a detailed comparison between the CFPP and the introduced IFPP scenarios, as presented in Table 10, several key observations are obtained. Firstly, the reference IFPP showcases a significantly higher fuel mass flow of 220 kg s^{-1}, four times that of the CFPP. However, it is interesting to note that the air mass flow for the reference IFPP is reduced to 494 kg s^{-1}, a considerable decrease from the CFPP's 677 kg s^{-1}. This shift in mass flows underscores the operational differences between the two configurations. Furthermore, the efficiency metrics, introduced in Section 6, reveal that the reference IFPP shows a net efficiency increase of 1.9 percentage points over the CFPP. This enhancement can be attributed to two primary factors: a higher auxiliary efficiency, which benefits from the elimination of mills and fuel gas desulfurization requirements, and an improved boiler efficiency. The latter sees a significant reduction in flue gas losses (β_{fg}), dropping from 5.2% in the CFPP to 1.1% in the reference IFPP. Nonetheless, the IFPP does not solely present advantages. The turbine/generator efficiency in the reference IFPP is slightly lower at 50.0% compared to the CFPP's 51.3%. This reduction is a consequence of integrating the surplus heat from the flue gas into a condensate side stream.

The introduced non-idealities for the IFPP operation lead to net efficiency penalties ranging from 0.4 to 0.8 percentage points when compared to the reference IFPP. Despite these penalties, the efficiencies remain superior to the reference CFPP by 1.1 to 1.5 percentage points. The scenario involving pre-oxidized iron with constrained conversion to magnetite results in a modest net efficiency penalty of 0.4 percentage points. This slight reduction can be explained by the assumption of a circular fuel flow, which does not associate the residual chemical energy in the main iron oxide stream exiting the power plant with losses. Only the residual chemical energy within the slag contributes to losses due to unburned combustibles. When comparing temperature control scenarios, either by the equivalence ratio or by FGR, the FGR operation stands out. Both of them lead to significant higher resulting gas mass flows but temperature control by increasing the FGR mass flow offers elevated boiler and auxiliary efficiencies but also reduces the molar oxygen concentration to 13%, potentially mitigating nanoparticle formation.

Lastly, the IFPP introduces topological modifications to incorporate the excess heat in the flue gas into the steam cycle. Without the solid residual heat recovery and without integrating excess heat into the steam cycle, the net efficiency drops to 45.56%. While this is a significant decrease from the ideal scenario, it still represents a noteworthy improvement of 0.8 percentage points over the reference CFPP.

Fig. 12 presents a sensitivity analysis of the reference IFPP. On the left is a Tornado plot detailing the parameter ranges, while the Morris sensitivities are depicted on the right. For the Morris sensitivity evaluation, the oxygen equivalence ratio (λ_{O_2}) is set to 1.2. Additionally, a FGR rate, x_{FGR}, is defined, representing the ratio between FGR mass flow and total air mass flow.

Notably, the proportion of nanoparticles, represented by x_{nan}, show negligible influence on the net release efficiency. This is attributed to the utilization of the sensible heat they contain. The sensitivity related to the mass fraction of slag losses (x_{slag}) is moderate, stemming from the assumption that particle and flue gas temperatures are identical post-reaction. The influence would be pronounced if completely unburned particles were to settle in the ash hopper. The sensitivity regarding the reduction degree at the inlet reduction is very small. Assumptions about the cyclone's pressure drop, Δp_{cyc}, indicate moderate sensitivity. A rise in the cyclone's pressure drop from 0.05 bar to 0.1 bar results in a net efficiency reduction of roughly 0.27% (0.05 bar · 5.3 %/bar). The oxidation degree at the outlet, $X_{ox,out}$, exhibits a moderate to high sensitivity, with its mean and standard deviation suggesting significant non-linearities and interactions. The most influential factors are the oxygen equivalence ratio (λ_{O_2}) and the FGR rate (x_{FGR}). As described

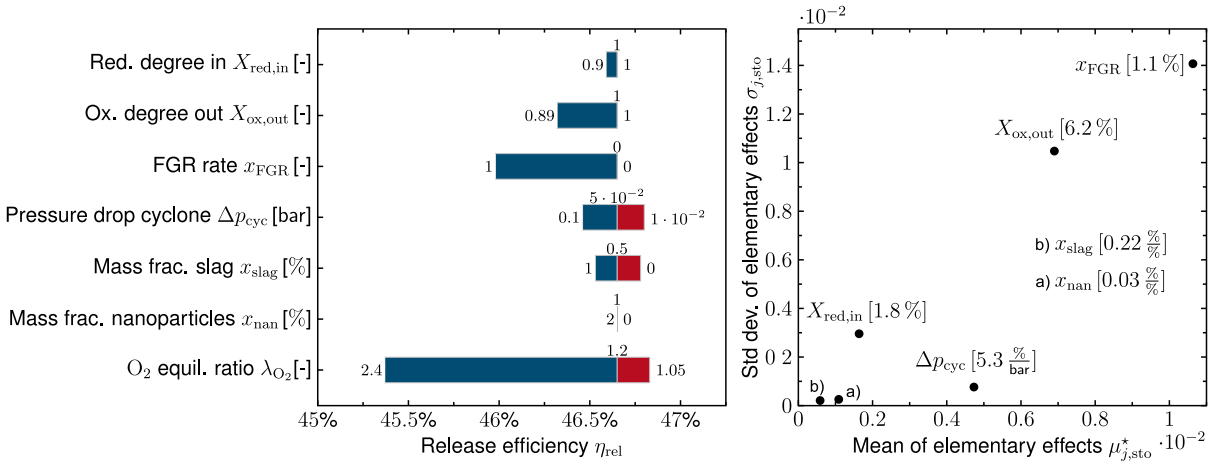

Fig. 12. Tornado plot (left) and Morris sensitivities (right) of selected parameters on the net release efficiency for the IFPP. The considered parameter intervals are given within the tornado plot. For the Morris screening, a constant oxygen equivalence ratio of $\lambda_{O_2} = 1.2$ is considered. The values next to data points in the right graph correspond to the absolute values of the mean of the elementary effects.

in more details in the IFPP operation scenario analysis, these operational parameters can be adjusted to modify combustion conditions (temperature and oxygen concentration) with moderate impacts on the net efficiency.

The in-depth evaluation of the IFPPs scenarios and sensitivities underscores the potential of IFPPs as a promising option for decarbonizing existing CFPPs (retrofit) by using green iron as fuel. This analysis demonstrates the resilience of IFPP configurations in surpassing CFPP efficiencies, even in suboptimal conditions.

It is worth mentioning that many CFPPs currently function as co-generation plants, frequently supplying heat for district heating systems. In such cases, transitioning to an IFPP is especially beneficial, fostering decarbonization across multiple sectors (both heat and electrical power). This transition ensures a carbon-neutral central heat supply, which is crucial for many contemporary district heating systems [161].

7.3. Overarching cycle

The comprehensive cycle evaluation, which includes storage of RE by either the SF-HDR or FR-HDR plants, intermediate storage, long-distance maritime transport, and release in IFPP, is based on a reference scenario, complemented by best and worst-case assumptions. These scenarios are detailed in Table 11. Parameters not explicitly mentioned are consistent with the previously established reference cases for the introduced IFPP and HDR plants. For the reference scenario, a transport distance of 5000 km is assumed. The analysis also accounts for losses during intermediate storage at both exporting and importing sites, as well as material losses. Material losses, whether due to mishandling or nanoparticle formation during the release phase, are replenished at the storage site. The energy demand, which covers mining, transport, and mineral processing for reference hematite mines in Australia, is set at 152.7 $\mathrm{MJ/t_{ore}}$ [162]. The results of the overarching iron-based energy cycle, including overall cycle efficiency and efficiencies of sub-processes, are illustrated in Fig. 13. This figure differentiates between the SF-HDR and FR-HDR plants for the storage process.

As previously highlighted in the individual assessment of the IFPP, the net release efficiency exhibits minor variations between 46.1% and 46.6% for both the best and worst-case scenarios. The reproduction efficiency is nearly 100% across all scenarios, indicating that the additional energy demand for reproducing the EC due to nanoparticle formation or material losses is negligible. This aligns with the evaluation conducted by Norgate et al. [162], which emphasizes that the energy requirements for activities such as mining, transport, and mineral processing are insignificant for iron ore.

Table 11
Overview of reference, best, and worst case assumptions for the overarching cycle.

Parameter	Best	Ref.	Worst
Efficiency electrolyzer $\eta_{\mathrm{ely,LHV}}$ [%]	75	70	65
Reduction degree storage $X_{\mathrm{red,sto}}$ [−]	1.00	0.95	0.9
Oxidation interm. storage 1 $\Delta X_{\mathrm{is,1}}$ [%]	0.00	0.01	0.02
Oxidation interm. storage 2 $\Delta X_{\mathrm{is,2}}$ [%]	0.00	0.02	0.04
Transport distance d_{tra} [10^3 km]	0	5	10
Fuel demand ship fd_{tra} [kWh $(10^3\,\mathrm{km\,t_{cargo}})^{-1}$]	6	7	8
Oxidation degree release $X_{\mathrm{ox,rel}}$ [−]	1	0.95	0.90
Mass fraction nanoparticles x_{nan} [%]	0	1	2
Material losses x_{mat} [%]	0	0.5	1

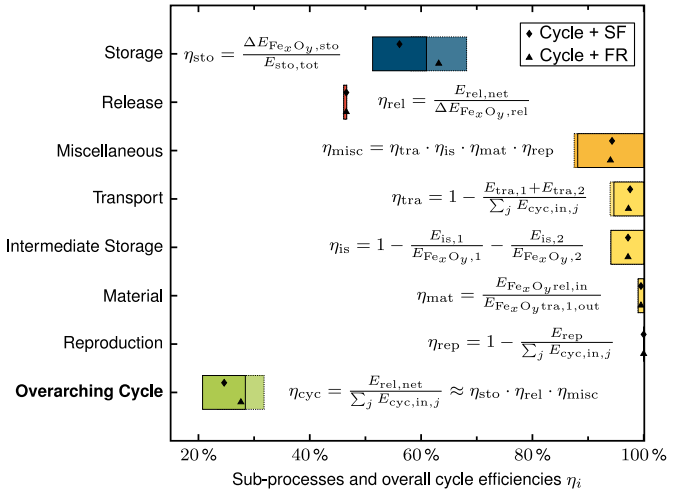

Fig. 13. Sub-processes and overall cycle efficiency considering FR-HDR and SF-HDR. The marks correspond to the reference parameterization and the interval to the best and worst assumptions provided in Table 11.

For the overarching cycle incorporating the FR-HDR plant, the best-case scenario is notably promising, with a storage efficiency of 68.2%. Under these conditions, the overall cycle efficiency reaches 31.8%. The worst-case scenario shows efficiencies of 58.2%, 94.1%, and 94.0% for net storage, intermediate storage, and transport, respectively. The overall cycle efficiency for this scenario is 23.4%. The reference scenario for the FR-HDR cycle shows efficiencies of 63.2%, 97.3%, and 97.2% for net storage, transport, and intermediate storage, respectively, leading to an overall cycle efficiency of 27.6%. The slight variance

in transport efficiency between the HDR plants is attributed to the efficiency definition of transport, which accounts for the total energy demand of the cycle, differing for both options.

For the overarching cycle incorporating the SF-HDR plant, the best-case scenario achieves a net storage efficiency of 61.0%. Under optimal conditions, such as no transport and no oxidation during intermediate storage, the overall cycle efficiency reaches 28.4%. The worst-case scenario yields a net storage efficiency of 51.3%, an intermediate storage efficiency of 94.1%, and a transport efficiency of 94.6%. In aggregate, the overall cycle efficiency for this scenario is 20.7%. The reference scenario for the SF-HDR cycle yields efficiencies of 56.1%, 97.6%, and 97.2% for net storage, transport, and intermediate storage, respectively. The overall cycle efficiency for this scenario is 24.6%.

The Morris sensitivity analysis for the overall cycle efficiency is presented in Fig. 14, accompanied by Table 12 detailing the absolute means of the elementary effects. The graph underscores that the overall behavior of the cycles incorporating either SF-HDR or FR-HDR is largely consistent with respect to the investigated parameters, except for the achieved reduction degree, which is significantly more pronounced for SF-HDR. This aligns with the prior assessment of the individual HDR plants. Notably, the electrolyzer efficiency exhibits high sensitivity in both cases, with absolute means of 0.38% for FR-HDR and 0.29% for SF-HDR. It is intriguing that oxidation during intermediate storage at reduction sites has a higher absolute mean compared to oxidation during intermediate storage at importing sites. This can be attributed to the amplified energy penalty propagation throughout the chain for unwanted oxidation at the exporting sites and the nonlinear relationship between the oxidation degree and the heating value of the EC. As observed in the scenario analysis above, the energetic impact of nanoparticles is negligible.

This in-depth analysis offers a clear insight into the efficiencies and sensitivities inherent to the iron-based energy cycle that integrates both SF-HDR and FR-HDR plants. The evaluation highlights that the greatest potential for enhancement lies within the HDR concept, with FR-HDR consistently outperforming SF-HDR. Additionally, electrolyzer efficiency and the minimizing of unwanted oxidation during intermediate storage emerge as most important. It is worth noting that transport distance remains a fixed factor, determined by the chosen storage site.

The derived power-to-power efficiencies for the investigated iron-based energy cycle are in the same order of magnitude as in recent assessments of using hydrogen or ammonia as green ECs (20-30%, [163]). However, the literature on alternative ECs shows considerable differences in assumptions. A thorough and fair comparison between alternative ECs requires normalization of these assumptions, which should be explored in future work. The results of this study, especially the provided reference points in conjunction with the specified sensitivities, serve as a valuable framework for estimating the cycle efficiency across different operational scenarios. This framework could be crucial in future research to identify the role of iron within the context of global-scale energy system modeling and assessments.

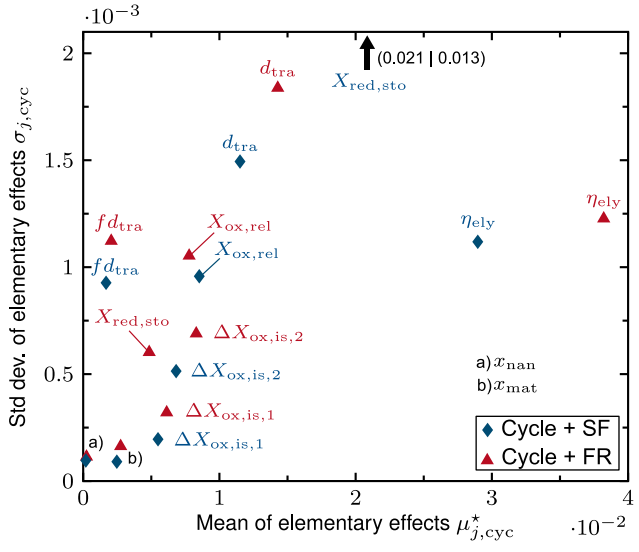

Fig. 14. Morris sensitivity for the overarching cycle considering FR-HDR and SF-HDR plants, considering the process parameters and intervals in Table 11.

8. Conclusion

The transition to a sustainable energy economy requires innovative solutions for the transport, long-term storage, and on-demand supply of renewable energy. While short-term energy storage, such as batteries, are increasingly prevalent, bridging day-night cycles and brief periods of renewable energy scarcity, there remains a significant gap in large scale seasonal energy storage solutions. These are essential for overcoming the challenges of reduced renewable energy availability during extended periods, particularly during the winter months, when solar activity is low for extended periods while demand is high. In this context, green energy carriers like hydrogen, ammonia, or iron present viable options. Iron, in particular, has a high volumetric energy density at ambient temperature and pressure and is non-toxic, making it an exceptional energy carrier. Moreover, an iron-based circular energy economy for carbon-free energy supply offers synergies with the decarbonization of the steel industry and benefits from the reuse of existing infrastructure. This alignment can lead to significant cost savings and reduced implementation times. Current advancements in the steel industry are focused on green reduction processes utilizing hydrogen, which are often denoted as “no-regret” applications for green hydrogen. These processes are expected to become economically viable and widely adopted within the coming decade(s). When integrated with the repurposing of existing transportation and electricity generation infrastructure – such as retrofitting coal-fired power plants – the iron-based energy cycle investigated in this study also emerges as a “no-regret” option. This approach serves multiple purposes: it mitigates the challenges associated with local renewable energy scarcity, enables long-term energy storage, and promotes power security.

Despite the growing interest in iron as an energy carrier, the literature features only few initial cycle evaluations. This study addresses this deficiency by developing and assessing comprehensive thermodynamic models for the individual sub-processes and the overarching iron-based energy cycle. Moreover, thorough sensitivity analyses have been performed to identify critical sub-processes and their respective parameters. Subsequently, the key finding are highlighted.

Storage of renewable energy: The flash reactor hydrogen direct reduction is superior to the shaft furnace hydrogen direct reduction (63.7% vs. 57.3% net storage efficiency for a reference case), primarily by sidestepping additional particle size alignment processes. Sensitivity analyses identify the electrolyzer efficiency as important for both hydrogen direct reduction plants, the achieved reduction degree for the shaft furnace concept, and heat recovery measures for the flash reactor concept.

Transport and intermediate storage: Iron and iron oxide fines can be transported, stored, and handled using established protocols for bulk solids. Existing infrastructure can be utilized (e.g. existing bulk solid vessels) rather than building a new fleet (e.g. as required for hydrogen transport), which might take decades. The extent of unwanted re-oxidation of the iron (oxides) can differ based on handling methods (i.e. low versus high effort). This undesired depletion affects the net cycle efficiency at the reduction sites more significantly than at the oxidation sites, due to increased energy demand for the transport and additional inefficiencies during the release.

Release of renewable energy: The transformation of coal-fired power plants (CFPPs) to iron-fired power plants (IFPPs) is thermodynamically

Table 12
Absolute values of the Morris sensitivity means for the overarching cycle.

Parameter	Electrolyzer efficiency	Red. degree storage	Oxidation during intermediate storage		Ox. degree release	Material losses	Nanoparticle formation	Transport distance	Specific fuel demand
	η_{ely} [%]	$X_{red,sto}$ [−]	$\Delta X_{ox,is,1}$ [−]	$\Delta X_{ox,is,2}$ [−]	$X_{ox,rel}$ [−]	x_{mat} [−]	x_{nan} [−]	d_{tra} [10^3 km]	$f d_{tra}$ [a]
Cycle + FR	0.38%	4.8%	30.6%	20.7%	7.8%	27.5%	1.2%	0.14%	0.1%
Cycle + SF	0.29%	21.4%	27.5%	17.0%	8.5%	24.6%	1.0%	0.12%	0.08%

[a] kWh/(10^3 km t).

advantageous. The results showcase the capability of IFPPs to outperform CFPPs in net efficiencies (up to 2 percentage points), even under less-than-ideal conditions such as incomplete conversion or limitations on allowable combustion temperatures. For the latter, flue gas recirculation appears to be a promising option for matching combustion conditions to potential requirements.

Overarching cycle: For the overarching cycle, net efficiencies (power-to-power) range from 24.6% to 28.4% for the SF-HDR and 27.6% to 31.8% for the FR-HDR considering reference and best case assumptions. Notably, from an energetic point of view, the formation of nanoparticles does not have a meaningful impact on the cycle efficiency.

As the global need for renewable energy on demand intensifies, energy carriers like iron offer promising solutions to balance demand and supply, especially in regions with limited self-sufficiency. The study highlights that an iron-based circular energy economy is not just a viable option but one that deserves increased focus, further research, and investment. Given its unique attributes and compatibility with existing industries and infrastructure, iron is well-suited to play a significant role in the transition to a more sustainable, reliable energy future.

CRediT authorship contribution statement

Jannik Neumann: Writing – review & editing, Writing – original draft, Visualization, Validation, Software, Methodology, Investigation, Formal analysis, Data curation, Conceptualization. **Quentin Fradet:** Writing – review & editing, Writing – original draft, Validation, Methodology, Investigation, Conceptualization. **Arne Scholtissek:** Writing – review & editing, Writing – original draft, Validation, Methodology, Investigation, Conceptualization. **Frank Dammel:** Writing – review & editing, Supervision, Methodology, Conceptualization. **Uwe Riedel:** Writing – review & editing, Supervision, Resources, Project administration, Methodology, Conceptualization. **Andreas Dreizler:** Writing – review & editing, Supervision, Resources, Project administration, Methodology, Funding acquisition, Conceptualization. **Christian Hasse:** Writing – review & editing, Supervision, Resources, Project administration, Methodology, Conceptualization. **Peter Stephan:** Writing – review & editing, Supervision, Resources, Project administration, Methodology, Funding acquisition, Conceptualization.

Declaration of competing interest

The authors declare that they have no known competing financial interests or personal relationships that could have appeared to influence the work reported in this paper.

Data availability

Data will be made available on request.

Declaration of Generative AI and AI-assisted technologies in the writing process

During the preparation of this work, the author(s) used DeepL, Grammarly, and ChatGPT in order to improve readability and language. After using these tools, the author(s) reviewed and edited the content as needed and take full responsibility for the content of the publication.

Acknowledgments

Funded by the Hessian Ministry of Higher Education, Research, Science and the Arts - cluster project Clean Circles.

References

[1] IPCC. Synthesis report of the IPCC sixth assessment report (AR6): Summary for policymakers. 2023, URL https://report.ipcc.ch/ar6syr/pdf/IPCC_AR6_SYR_SPM.pdf.
[2] Callahan CW, Mankin JS. Globally unequal effect of extreme heat on economic growth. Sci Adv 2022;8(43). http://dx.doi.org/10.1126/sciadv.add3726.
[3] Lenton TM, Xu C, Abrams JF, Ghadiali A, Loriani S, Sakschewski B, Zimm C, Ebi KL, Dunn RR, Svenning J-C, Scheffer M. Quantifying the human cost of global warming. Nat Sustain 2023. http://dx.doi.org/10.1038/s41893-023-01132-6.
[4] Gielen D, Boshell F, Saygin D, Bazilian MD, Wagner N, Gorini R. The role of renewable energy in the global energy transformation. Energy Strategy Rev 2019;24:38–50. http://dx.doi.org/10.1016/j.esr.2019.01.006.
[5] IEA, International Energy Agency. CO2 emissions in 2022. 2022, URL https://iea.blob.core.windows.net/assets/525166b4-1201-47bf-8413-9cf3fededbfd/CO2Emissionsin2022.pdf.
[6] Ember. Global-electricity-review-2023. 2023, URL https://ember-climate.org/insights/research/global-electricity-review-2023/#supporting-material-downloads.
[7] Global Energy Monitor. Dashboard - global energy monitor. 2023, URL https://globalenergymonitor.org/projects/global-coal-plant-tracker/dashboard/.
[8] UNFCCC. The Paris agreement. 2016, URL https://unfccc.int/sites/default/files/resource/parisagreement_publication.pdf?download.
[9] COP26, United Nations Climate Change Conference. End of coal in sight at COP26 | UNFCCC. 2021, URL https://unfccc.int/news/end-of-coal-in-sight-at-cop26.
[10] International Energy Agency. The role of low-carbon fuels in the clean energy transitions of the power sector. 2021, URL https://www.iea.org/reports/the-role-of-low-carbon-fuels-in-the-clean-energy-transitions-of-the-power-sector.
[11] Schnuelle C, Thoeming J, Wassermann T, Thier P, von Gleich A, Goessling-Reisemann S. Socio-technical-economic assessment of power-to-X: Potentials and limitations for an integration into the german energy system. Energy Res Soc Sci 2019;51:187–97. http://dx.doi.org/10.1016/j.erss.2019.01.017.
[12] Dreizler A, Pitsch H, Scherer V, Schulz C, Janicka J. The role of combustion science and technology in low and zero impact energy transformation processes. Appl Energy Combust Sci 2021;7:100040. http://dx.doi.org/10.1016/j.jaecs.2021.100040.
[13] Hydrogen Council. Hydrogen in decarbonized energy systems. 2023, URL https://hydrogencouncil.com/en/hydrogen-in-decarbonized-energy-systems/.
[14] Federal Ministry for Economic Affairs and Climate Action. Electricity storage strategy. 2023, URL https://www.bmwk.de/Redaktion/DE/Publikationen/Energie/electricity-storage-strategy.pdf?_blob=publicationFile&v=6.
[15] Bundesnetzagentur. Press release: 2023 electricity market data. 2024, URL https://www.bundesnetzagentur.de/SharedDocs/Pressemitteilungen/EN/2024/20240103_SMARD.html?nn=666514#ANKER.
[16] AG Energiebilanzen eV. Energy flow chart for the federal rebulic of Germany in 2022. 2022, URL https://ag-energiebilanzen.de/wp-content/uploads/2023/09/AGEB_Energieflussbild-kurz_ENG-2022-PJ_20230920.pdf.
[17] Wiese F, Thema J, Cordroch L. Strategies for climate neutrality. Lessons from a meta-analysis of german energy scenarios. Renew Sustain Energy Transit 2022;2:100015. http://dx.doi.org/10.1016/j.rset.2021.100015.
[18] Gür TM. Review of electrical energy storage technologies, materials and systems: challenges and prospects for large-scale grid storage. Energy Environ Sci 2018;11(10):2696–767. http://dx.doi.org/10.1039/C8EE01419A.
[19] Schmidt J, Gruber K, Klingler M, Klöckl C, Ramirez Camargo L, Regner P, Turkovska O, Wehrle S, Wetterlund E. A new perspective on global renewable energy systems: why trade in energy carriers matters. Energy Environ Sci 2019;12(7):2022–9. http://dx.doi.org/10.1039/C9EE00223E.
[20] Egerer J, Grimm V, Niazmand K, Runge P. The economics of global green ammonia trade – "shipping Australian wind and sunshine to Germany". Appl Energy 2023;334:120662. http://dx.doi.org/10.1016/j.apenergy.2023.120662.

[21] Pfennig M, Böttger D, Häckner B, Geiger D, Zink C, Bisevic A, Jansen L. Global GIS-based potential analysis and cost assessment of power-to-X fuels in 2050. Appl Energy 2023;347:121289. http://dx.doi.org/10.1016/j.apenergy.2023.121289, URL https://www.sciencedirect.com/science/article/pii/S0306261923006530.

[22] Crandall BS, Brix T, Weber RS, Jiao F. Techno-economic assessment of green H 2 carrier supply chains. Energy Fuels 2022. http://dx.doi.org/10.1021/acs.energyfuels.2c03616.

[23] Christoph Hank, Marius Holst, Connor Thelen, Christoph Kost, Sven Längle, Achim Schaadt, Tom Smolinka. Power-to-X country analysis: Site-specific, comparative analysis for suitable power-to-X pathways and products in developing and emerging countries. 2023, URL https://www.ise.fraunhofer.de/en/publications/studies/power-to-x-country-analyses.html.

[24] Hampp J, Düren M, Brown T. Import options for chemical energy carriers from renewable sources to Germany. PLoS One 2023;18(2):e0262340. http://dx.doi.org/10.1371/journal.pone.0281380.

[25] Tsiklios C, Hermesmann M, Müller TE. Hydrogen transport in large-scale transmission pipeline networks: Thermodynamic and environmental assessment of repurposed and new pipeline configurations. Appl Energy 2022;327:120097. http://dx.doi.org/10.1016/j.apenergy.2022.120097.

[26] Schuler J, Ardone A, Fichtner W. A review of shipping cost projections for hydrogen-based energy carriers. Int J Hydrog Energy 2023. http://dx.doi.org/10.1016/j.ijhydene.2023.10.004.

[27] Cheng W, Lee S. How green are the national hydrogen strategies? Sustainability 2022;14(3):1930. http://dx.doi.org/10.3390/su14031930.

[28] Wolf A, Zander N. Green hydrogen in Europe: Do strategies meet expectations? Intereconomics 2021;56(6):316–23. http://dx.doi.org/10.1007/s10272-021-1008-3.

[29] Plank F, Daum B, Muntschick J, Knodt M, Hasse C, Ott I, Niemann A. Hydrogen: Fueling EU–Morocco energy cooperation? Middle East Policy 2023. http://dx.doi.org/10.1111/mepo.12699.

[30] Flath L, Kemmerzell J, Knodt M. Hydrogen governance in Germany: a challenge for federal coordination. Reg Fed Stud 2023;1–23. http://dx.doi.org/10.1080/13597566.2023.2232735.

[31] DOE. Funding opportunities : DOE hydrogen program. 2023, URL https://www.hydrogen.energy.gov/funding_opportunities.html.

[32] Internal Market, Industry, Entrepreneurship and SMEs. EU funding programmes and funds. 2023, URL https://single-market-economy.ec.europa.eu/industry/strategy/hydrogen/funding-guide/eu-programmes-funds_en.

[33] Bergthorson JM, Goroshin S, Soo MJ, Julien P, Palecka J, Frost DL, Jarvis DJ. Direct combustion of recyclable metal fuels for zero-carbon heat and power. Appl Energy 2015;160:368–82. http://dx.doi.org/10.1016/j.apenergy.2015.09.037.

[34] Bergthorson JM, Yavor Y, Palecka J, Georges W, Soo M, Vickery J, Goroshin S, Frost DL, Higgins AJ. Metal-water combustion for clean propulsion and power generation. Appl Energy 2017;186:13–27. http://dx.doi.org/10.1016/j.apenergy.2016.10.033.

[35] Bergthorson JM. Recyclable metal fuels for clean and compact zero-carbon power. Prog Energy Combust Sci 2018;68:169–96. http://dx.doi.org/10.1016/j.pecs.2018.05.00.

[36] Wiinikka H, Vikström T, Wennebro J, Toth P, Sepman A. Pulverized sponge iron, a zero-carbon and clean substitute for fossil coal in energy applications. Energy Fuels 2018;32(9):9982–9. http://dx.doi.org/10.1021/acs.energyfuels.8b02270.

[37] Debiagi P, Rocha RC, Scholtissek A, Janicka J, Hasse C. Iron as a sustainable chemical carrier of renewable energy: Analysis of opportunities and challenges for retrofitting coal-fired power plants. Renew Sustain Energy Rev 2022;165:112579. http://dx.doi.org/10.1016/j.rser.2022.112579.

[38] Trowell KA, Goroshin S, Frost DL, Bergthorson JM. Aluminum and its role as a recyclable, sustainable carrier of renewable energy. Appl Energy 2020;275:115112. http://dx.doi.org/10.1016/j.apenergy.2020.115112.

[39] Neumann J, Da Rocha RC, Debiagi P, Scholtissek A, Dammel F, Stephan P, Hasse C. Techno-economic assessment of long-distance supply chains of energy carriers: Comparing hydrogen and iron for carbon-free electricity generation. Appl Energy Combust Sci 2023;14:100128. http://dx.doi.org/10.1016/j.jaecs.2023.100128.

[40] Jansen E, Schuler J, Ardone A, Slednev V, Fichtner W, Pfetsch ME. Global logistics of an iron-based energy network: A case study of retrofitting german coal power plants: Working paper. 2023, http://dx.doi.org/10.5445/IR/1000158253.

[41] Eindhoven University of Technology, Metalot, Pometon, EM Group, RISE ETC, Shell, SOLID, RIFT, Veolia, HeatPower. Iron power ecosystem: A clean and circular energy carrier. 2022, URL https://www.metalot.nl/pdf/Vision%20document%20Iron%20Power%20juni2022.pdf.

[42] Janicka J, Debiagi P, Scholtissek A, Dreizler A, Epple B, Pawellek R, Maltsev A, Hasse C. The potential of retrofitting existing coal power plants: A case study for operation with green iron. Appl Energy 2023;339:120950. http://dx.doi.org/10.1016/j.apenergy.2023.120950.

[43] Raabe D. The materials science behind sustainable metals and alloys. Chem Rev 2023;123(5):2436–608. http://dx.doi.org/10.1021/acs.chemrev.2c00799.

[44] Vogl V, Åhman M, Nilsson LJ. Assessment of hydrogen direct reduction for fossil-free steelmaking. J Clean Prod 2018;203:736–45. http://dx.doi.org/10.1016/j.jclepro.2018.08.279.

[45] Bhaskar A, Assadi M, Nikpey Somehsaraei H. Decarbonization of the iron and steel industry with direct reduction of iron ore with green hydrogen. Energies 2020;13(3):758. http://dx.doi.org/10.3390/en13030758.

[46] Lopez G, Farfan J, Breyer C. Trends in the global steel industry: Evolutionary projections and defossilisation pathways through power-to-steel. J Clean Prod 2022;375:134182. http://dx.doi.org/10.1016/j.jclepro.2022.134182.

[47] Rechberger K, Spanlang A, Sasiain Conde A, Wolfmeir H, Harris C. Green hydrogen–based direct reduction for low–carbon steelmaking. Steel Res Int 2020;91(11):2000110. http://dx.doi.org/10.1002/srin.202000110.

[48] Agora Industry and Wuppertal Institute. 15 Insights on the global steel transformation. 2023, URL https://static.agora-energiewende.de/fileadmin/Projekte/2021/2021-06_IND_INT_GlobalSteel/A-EW_298_GlobalSteel_Insights_WEB.pdf.

[49] Wang RR, Zhao YQ, Babich A, Senk D, Fan XY. Hydrogen direct reduction (H-DR) in steel industry—An overview of challenges and opportunities. J Clean Prod 2021;329:129797. http://dx.doi.org/10.1016/j.jclepro.2021.129797.

[50] Sohn HY. Flash Ironmaking. Boca Raton: CRC Press; 2023.

[51] Devlin A, Kossen J, Goldie-Jones H, Yang A. Global green hydrogen-based steel opportunities surrounding high quality renewable energy and iron ore deposits. Nat Commun 2023;14(1):2578. http://dx.doi.org/10.1038/s41467-023-38123-2.

[52] United Nations. The united nations world water development report 2023: Partnerships and cooperation for water: Executive summary. 2023, URL https://unesdoc.unesco.org/ark:/48223/pf0000384657.

[53] Dirven L, Deen NG, Golombok M. Dense energy carrier assessment of four combustible metal powders. Sustain Energy Technol Assess 2018;30:52–8. http://dx.doi.org/10.1016/j.seta.2018.09.003.

[54] Kuhn C, Düll A, Rohlfs P, Tischer S, Börnhorst M, Deutschmann O. Iron as recyclable energy carrier: Feasibility study and kinetic analysis of iron oxide reduction. Appl Energy Combust Sci 2022;12:100096. http://dx.doi.org/10.1016/j.jaecs.2022.100096.

[55] Iqony GmbH. EBSILON professional. 2023, URL https://www.ebsilon.com/en/.

[56] McBride BJ, Zehe MJ, Gordon S. NASA glenn coefficients for calculating thermodynamic properties of individual species. 2002, URL https://ntrs.nasa.gov/citations/20020085330.

[57] Bale CW, Bélisle E, Chartrand P, Decterov SA, Eriksson G, Gheribi AE, Hack K, Jung I-H, Kang Y-B, Melançon J, Pelton AD, Petersen S, Robelin C, Sangster J, Spencer P, van Ende M-A. FactSage thermochemical software and databases, 2010–2016. CALPHAD 2016;54:35–53. http://dx.doi.org/10.1016/j.calphad.2016.05.002.

[58] IEA. Global crude steel production by process route and scenario, 2019–2050 – charts – data & statistics - IEA. 2023, URL https://www.iea.org/data-and-statistics/charts/global-crude-steel-production-by-process-route-and-scenario-2019-2050.

[59] Sohn HY. Energy consumption and CO2 emissions in ironmaking and development of a novel flash technology. Metals 2020;10(1):54. http://dx.doi.org/10.3390/met10010054.

[60] Spreitzer D, Schenk J. Reduction of iron oxides with hydrogen—A review. Steel Res Int 2019;90(10):1900108. http://dx.doi.org/10.1002/srin.201900108.

[61] Gavarri J-R, Carel C. The complex nonstoichiometry of Wüstite Fe1-O: Review and comments. Prog Solid State Chem 2019;53:27–49. http://dx.doi.org/10.1016/j.progsolidstchem.2018.10.001.

[62] Spreitzer D, Schenk J. Iron ore reduction by hydrogen using a laboratory scale fluidized bed reactor: Kinetic investigation—Experimental setup and method for determination. Metall Mater Trans B 2019;50(5):2471–84. http://dx.doi.org/10.1007/s11663-019-01650-9.

[63] Fradet Q, Kurnatowska M, Riedel U. Thermochemical reduction of iron oxide powders with hydrogen: Review of selected thermal analysis studies. Thermochim Acta 2023;726:179552. http://dx.doi.org/10.1016/j.tca.2023.179552.

[64] Patisson F, Mirgaux O. Hydrogen ironmaking: How it works. Metals 2020;10(7):922. http://dx.doi.org/10.3390/met10070922.

[65] Midrex Technologies Inc. 2021 World direct reduction statistics. 2021, URL https://www.midrex.com/wp-content/uploads/MidrexSTATSBook2021.pdf.

[66] Fan Z, Friedmann SJ. Low-carbon production of iron and steel: Technology options, economic assessment, and policy. Joule 2021;5(4):829–62. http://dx.doi.org/10.1016/j.joule.2021.02.018.

[67] Nuber D, Eichberger H, Rollinger B. Circored fine ore direct reduction. Stahl Eisen 2006;126(4).

[68] Yi S-H, Choi M-E, Kim D-H, Ko C-K, Park W-I, Kim S-Y. FINEX® as an environmentally sustainable ironmaking process. Ironmak Steelmak 2019;46(7):625–31. http://dx.doi.org/10.1080/03019233.2019.1641682.

[69] Schenk JL. Recent status of fluidized bed technologies for producing iron input materials for steelmaking. Particuology 2011;9(1):14–23. http://dx.doi.org/10.1016/j.partic.2010.08.011.

[70] Wolfinger T, Spreitzer D, Schenk J. Using iron ore ultra-fines for hydrogen-based fluidized bed direct reduction-a mathematical evaluation. Materials 2022;15(11). http://dx.doi.org/10.3390/ma15113943.

[71] Wolfinger T, Spreitzer D, Schenk J. Analysis of the usability of iron ore ultra-fines for hydrogen-based fluidized bed direct reduction-a review. Materials 2022;15(7). http://dx.doi.org/10.3390/ma15072687.

[72] Guo L, Bao Q, Gao J, Zhu Q, Guo Z. A review on prevention of sticking during fluidized bed reduction of fine iron ore. ISIJ Int 2020;60(1):1–17. http://dx.doi.org/10.2355/isijinternational.ISIJINT-2019-392.

[73] Liu X, Zhang X, Li J, Zhu Q, Deen NG, Tang Y. Regeneration of iron fuel in fluidized beds part II: Reduction experiments. Powder Technol 2023;420:118183. http://dx.doi.org/10.1016/j.powtec.2022.118183.

[74] Lopes DV, Quina MJ, Frade JR, Kovalevsky AV. Prospects and challenges of the electrochemical reduction of iron oxides in alkaline media for steel production. Front Mater 2022;9. http://dx.doi.org/10.3389/fmats.2022.1010156.

[75] European Commission, Directorate-General for Research, Innovation, Olsen K, van der Laan S, Lavelaine de Maubeuge H, Serna M, Hita A, Haarberg G, Frade J. Iron production by electrochemical reduction of its oxide for high CO2 mitigation (IERO) – Final report. Publications Office; 2016, http://dx.doi.org/10.2777/084034.

[76] Fischedick M, Marzinkowski J, Winzer P, Weigel M. Techno-economic evaluation of innovative steel production technologies. J Clean Prod 2014;84:563–80. http://dx.doi.org/10.1016/j.jclepro.2014.05.063.

[77] Wiencke J, Lavelaine H, Panteix P-J, Petitjean C, Rapin C. Electrolysis of iron in a molten oxide electrolyte. J Appl Electrochem 2018;48(1):115–26. http://dx.doi.org/10.1007/s10800-017-1143-5.

[78] Allanore A, Lavelaine H, Valentin G, Birat JP, Lapicque F. Electrodeposition of metal iron from dissolved species in alkaline media. J Electrochem Soc 2007;154(12):E187. http://dx.doi.org/10.1149/1.2790285.

[79] Allanore A, Lavelaine H, Valentin G, Birat JP, Lapicque F. Iron metal production by bulk electrolysis of iron ore particles in aqueous media. J Electrochem Soc 2008;155(9):E125. http://dx.doi.org/10.1149/1.2952547.

[80] Majid AI, Finotello G, van der Schaaf J, Deen NG, Tang Y. On the formation of dendritic iron from alkaline electrochemical reduction of iron oxide prepared for metal fuel applications. Chem Eng Sci 2024;291:119931. http://dx.doi.org/10.1016/j.ces.2024.119931.

[81] Lausch M, Brockmann P, Schmitt F, Etzold B, Hussong J. In-situ iron oxide particle size and shape evolution during the dissolution in oxalic acid. Chem Eng Sci 2024;289:119864. http://dx.doi.org/10.1016/j.ces.2024.119864.

[82] Bhagat RP. Agglomeration of iron ores. Boca Raton: CRC Press Taylor & Francis; 2019.

[83] Seetharaman S. Treatise on process metallurgy, Volume 3. Burlington: Elsevier Science; 2013, URL https://ebookcentral.proquest.com/lib/kxp/detail.action?docID=1582318.

[84] de Moraes SL, de Lima JRB, Ribeiro TR. Iron ore pelletizing process: An overview. In: Shatokha V, editor. Iron ores and iron oxide materials. InTech; 2018, p. 416. http://dx.doi.org/10.5772/intechopen.73164.

[85] Lohmeier L, Thaler C, Harris C, Wollenberg R, Schröder H-W, Braeuer AS. Use of bentonite and organic binders in the briquetting of particulate residues from the midrex process for improving the thermal stability and reducibility of the briquettes. Steel Res Int 2021;92(11):2100210. http://dx.doi.org/10.1002/srin.202100210.

[86] Wiinikka H, Sepman A, Ögren Y, Lindblom B, Nordin L-O. Combustion evaluation of renewable fuels for iron-ore pellet induration. Energy Fuels 2019;33(8):7819–29. http://dx.doi.org/10.1021/acs.energyfuels.9b01356.

[87] Midrex Technologies I. 2022 World direct reduction statistics. 2023, URL https://www.midrex.com/wp-content/uploads/MidrexSTATSBook2022.pdf.

[88] Rosner F, Papadias DD, Brooks KP, Yoro K, Ahluwalia RK, Autrey T, Breunig H. Green steel: design and cost analysis of hydrogen-based direct iron reduction. Energy Environ Sci 2023. http://dx.doi.org/10.1039/D3EE01077E.

[89] Cavaliere P, Perrone A, Marsano D, Primavera V. Hydrogen-based direct reduction of iron oxides pellets modeling. Steel Res Int 2023;94(6):2200791. http://dx.doi.org/10.1002/srin.202200791.

[90] Fradet Q, Ali ML, Riedel U. Development of a porous solid model for the direct reduction of iron ore pellets. Steel Res Int 2022;93(12):2200042. http://dx.doi.org/10.1002/srin.202200042.

[91] Ali ML, Fradet Q, Riedel U. Kinetic mechanism development for the direct reduction of single hematite pellets in H2/CO atmospheres. Steel Res Int 2022;93(12):2200043. http://dx.doi.org/10.1002/srin.202200043.

[92] Metolina P, Ribeiro TR, Guardani R. Hydrogen-based direct reduction of industrial iron ore pellets: Statistically designed experiments and computational simulation. Int J Miner Metal Mater 2022;29(10):1908–21. http://dx.doi.org/10.1007/s12613-022-2487-3.

[93] Zare Ghadi A, Radfar N, Valipour MS, Sohn HY. A review on the modeling of direct reduction of iron oxides in gas–based shaft furnaces. Steel Res Int 2023. http://dx.doi.org/10.1002/srin.202200742.

[94] Rocha EPd, Castro JAd, Silva L, Caldas RdS. Computational analysis of the performance of shaft furnaces with partial replacement of the burden with self-reducing pellets containing biomass. Mater Res 2019;22(6):e20190533. http://dx.doi.org/10.1590/1980-5373-MR-2019-0533.

[95] Zare Ghadi A, Valipour MS, Biglari M. CFD simulation of two-phase gas-particle flow in the midrex shaft furnace: The effect of twin gas injection system on the performance of the reactor. Int J Hydrog Energy 2017;42(1):103–18. http://dx.doi.org/10.1016/j.ijhydene.2016.11.053.

[96] Hamadeh H, Mirgaux O, Patisson F. Detailed modeling of the direct reduction of iron ore in a shaft furnace. Materials 2018;11(10). http://dx.doi.org/10.3390/ma11101865.

[97] Ranzani da Costa A, Wagner D, Patisson F. Modelling a new, low CO2 emissions, hydrogen steelmaking process. J Clean Prod 2013;46:27–35. http://dx.doi.org/10.1016/j.jclepro.2012.07.045, Key Elements (Stages and Tools) for a Sustainable World.

[98] Dossett JL, Totten GE. ASM handbook: powder metal technologies and applications. Vol. 7, Materials Park, Ohio: ASM International; 1998.

[99] Midrex Technologies. Hotlink® system: benefits of charging hot dri. 2014, URL https://www.midrex.com/wp-content/uploads/Hot_Transport_-_HOTLINK.pdf.

[100] Jorge Madias. Chapter 1.5 - electric furnace steelmaking. In: Seshadri Seetharaman, editor. Treatise on process metallurgy. Boston: Elsevier; 2014, p. 271–300. http://dx.doi.org/10.1016/B978-0-08-096988-6.00013-4.

[101] Kirschen M, Hay T, Echterhof T. Process improvements for direct reduced iron melting in the electric arc furnace with emphasis on slag operation. Processes 2021;9(2):402. http://dx.doi.org/10.3390/pr9020402.

[102] Dunkley JJ. Metal powder atomisation methods for modern manufacturing. Johns Matthey Technol Rev 2019;63(3):226–32. http://dx.doi.org/10.1595/205651319X15583434137356.

[103] Persson F, Eliasson A, Jönsson P. Prediction of particle size for water atomised metal powders: parameter study. Powder Metall 2012;55(1):45–53. http://dx.doi.org/10.1179/1743290111Y.0000000016.

[104] Nasr GG, Yule AJ, Bendig L. Industrial sprays and atomization: design, analysis and applications. London: Springer; 2002.

[105] Neumann J, Dammel F, Stephan P. Advanced exergy analysis of the flash ironmaking process. In: Smith JR, editor. 36th international conference on efficiency, cost, optimization, simulation and environmental impact of energy systems. ECOS 2023, Las Palmas De Gran Canaria, Spain: ECOS 2023; 2020, p. 160–71. http://dx.doi.org/10.52202/069564-0016.

[106] Chen F, Mohassab Y, Jiang T, Sohn HY. Hydrogen reduction kinetics of hematite concentrate particles relevant to a novel flash ironmaking process. Metall Mater Trans B 2015;46(3):1133–45. http://dx.doi.org/10.1007/s11663-015-0332-z.

[107] Sohn HY, Fan D-Q, Abdelghany A. Design of novel flash ironmaking reactors for greatly reduced energy consumption and CO2 emissions. Metals 2021;11(2):332. http://dx.doi.org/10.3390/met11020332.

[108] Sohn HY, Elzohiery M, Fan D-Q. Development of the flash ironmaking technology (FIT) for green ironmaking with low energy consumption. J Energy Power Technol 2021;03(03):1. http://dx.doi.org/10.21926/jept.2103042.

[109] Zhong Y-W, Wang Z, Gong X-Z, Guo Z-C. Sticking behavior caused by sintering in gas fluidisation reduction of haematite. Ironmak Steelmak 2012;39(1):38–44. http://dx.doi.org/10.1179/1743281211Y.0000000051.

[110] Hessels C, Smeets A, Finotello G, Deen NG, Tang Y. Sintering behavior of combusted iron powder in a packed bed reactor with nitrogen and hydrogen. Particuology 2023;83:8–17. http://dx.doi.org/10.1016/j.partic.2023.02.007.

[111] Yi L, Huang Z, Jiang T. Sticking of iron ore pellets during reduction with hydrogen and carbon monoxide mixtures: Behavior and mechanism. Powder Technol 2013;235:1001–7. http://dx.doi.org/10.1016/j.powtec.2012.11.043.

[112] Wang G, Zhang J, Li Y, Xu C, Liu Z. Study on sticking mechanism of pellets under low H2/CO conditions. Powder Technol 2019;352:25–31. http://dx.doi.org/10.1016/j.powtec.2019.04.026.

[113] Di Z-x, Li Z-y, Wei R-f, Liu Y, Meng Q-m, Chun T-j, Long H-m, Li J-x, Wang P. Sticking behaviour and mechanism of iron ore pellets in COREX pre-reduction shaft furnace. Ironmak Steelmak 2019;46(2):159–64. http://dx.doi.org/10.1080/03019233.2017.1361079.

[114] Wang X, Fu G, Li W, Zhu M. Numerical simulation of effect of operating conditions on flash reduction behaviour of magnetite under H2 atmosphere. Int J Hydrog Energy 2019;44(48):26261–70. http://dx.doi.org/10.1016/j.ijhydene.2019.08.089.

[115] Yuan Z, Sohn HY. Re-oxidation kinetics of flash reduced iron particles in O2–N2 gas mixtures relevant to a novel flash ironmaking process. ISIJ Int 2014;54(6):1235–43. http://dx.doi.org/10.2355/isijinternational.54.1235.

[116] Julien P, Bergthorson JM. Enabling the metal fuel economy: green recycling of metal fuels. Sustain Energy Fuels 2017;1(3):615–25. http://dx.doi.org/10.1039/C7SE00004A.

[117] Halter F, Jeanjean S, Chauveau C, Berro Y, Balat-Pichelin M, Brilhac JF, Andrieu A, Schonnenbeck C, Leyssens G, Dumand C. Recyclable metal fuels as future zero-carbon energy carrier. Appl Energy Combust Sci 2023;13:100100. http://dx.doi.org/10.1016/j.jaecs.2022.100100.

[118] Garra P, Leyssens G, Allgaier O, Schönnenbeck C, Tschamber V, Brilhac J-F, Tahtouh T, Guézet O, Allano S. Magnesium/air combustion at pilot scale and subsequent PM and NO x emissions. Appl Energy 2017;189:578–87. http://dx.doi.org/10.1016/j.apenergy.2016.12.069.

[119] Goroshin S, Palečka J, Bergthorson JM. Some fundamental aspects of laminar flames in nonvolatile solid fuel suspensions. Prog Energy Combust Sci 2022;57. http://dx.doi.org/10.1016/j.pecs.2022.100994.

[120] Julien P, Whiteley S, Goroshin S, Soo MJ, Frost DL, Bergthorson JM. Flame structure and particle-combustion regimes in premixed methane–iron–air suspensions. Proc Combust Inst 2015;35:2431–8. http://dx.doi.org/10.1016/j.proci.2014.05.003.

[121] Pál Tóth, Yngve Ögren, Alexey Sepman, Per Gren, Henrik Wiinikka. Combustion behavior of pulverized sponge iron as a recyclable electrofuel. Powder Technol 2020;373:210–9. http://dx.doi.org/10.1016/j.powtec.2020.05.078.

[122] Buchheiser S, Deutschmann MP, Rhein F, Allmang A, Fedoryk M, Stelzner B, Harth S, Trimis D, Nirschl H. Particle and phase analysis of combusted iron particles for energy storage and release. Materials (Basel, Switzerland) 2023;16(5). http://dx.doi.org/10.3390/ma16052009.

[123] Choisez L, van Rooij NE, Hessels CJ, Da Silva AK, Filho IRS, Ma Y, de Goey P, Springer H, Raabe D. Phase transformations and microstructure evolution during combustion of iron powder. Acta Mater 2022;239:118261. http://dx.doi.org/10.1016/j.actamat.2022.118261.

[124] Li T, Heck F, Reinauer F, Böhm B, Dreizler A. Visualizing particle melting and nanoparticle formation during single iron particle oxidation with multi-parameter optical diagnostics. Combust Flame 2022;245:112357. http://dx.doi.org/10.1016/j.combustflame.2022.112357.

[125] Ning D, Shoshin Y, Van Oijen JA, Finotello G, de Goey LP. Critical temperature for nanoparticle cloud formation during combustion of single micron-sized iron particle. Combust Flame 2022;244:112296. http://dx.doi.org/10.1016/j.combustflame.2022.112296.

[126] Baigmohammadi M, Prasidha W, Stevens NC, Shoshyn YL, Spee T, De Goey P. Towards utilization of iron powders for heating and power. Appl Energy Combust Sci 2023;13:100116. http://dx.doi.org/10.1016/j.jaecs.2023.100116.

[127] McRae M, Julien P, Salvo S, Goroshin S, Frost DL, Bergthorson JM. Stabilized, flat iron flames on a hot counterflow burner. Proc Combust Inst 2019;37:3185–91. http://dx.doi.org/10.1016/j.proci.2018.06.134.

[128] Fedoryk M, Stelzner B, Harth S, Trimis D. Experimental investigation of the laminar burning velocity of iron-air flames in a tube burner. Appl Energy Combust Sci 2023;13:100111. http://dx.doi.org/10.1016/j.jaecs.2022.100111.

[129] Krenn T, Li T, Hebel J, Böhm B, Dreizler A. Evaluation of a novel measurement method for the laminar burning speed in laminar lifted iron dust flames. Fuel 2024;366:131266. http://dx.doi.org/10.1016/j.fuel.2024.131266.

[130] World-Energy. Rheinhafen-dampfkraftwerk block 8 achieved a 47.5% net thermal efficiency. 2019, URL https://www.world-energy.org/article/1198.html.

[131] Tumanovskii AG, Shvarts AL, Somova EV, Verbovetskii EK, Avrutskii GD, Ermakova SV, Kalugin RN, Lazarev MV. Review of the coal-fired, over-supercritical and ultra-supercritical steam power plants. Therm Eng 2017;64(2):83–96. http://dx.doi.org/10.1134/S0040601517020082.

[132] International Energy Agency. Technology roadmap high efficiency low emissions coal fired power generation. 2013, URL https://iea.blob.core.windows.net/assets/c43bc244-0050-45ec-807c-d870ae9241a7/TechnologyRoadmapHighEfficiencyLowEmissionsCoalFiredPowerGeneration_WEB_Updated_March2013.pdf.

[133] Mich J, Braig D, Gustmann T, Hasse C, Scholtissek A. A comparison of mechanistic models for the combustion of iron microparticles and their application to polydisperse iron-air suspensions. Combust Flame 2023;256:112949. http://dx.doi.org/10.1016/j.combustflame.2023.112949.

[134] Spliethoff H. Power generation from solid fuels. Power systems, Heidelberg and New York: Springer; 2010.

[135] VDI e V. VDI heat atlas. VDI-buch, 2nd ed.. Berlin and New York: Springer; 2010.

[136] United Nations. Navigating stormy waters. Review of maritime transport / united nations conference on trade and development, Geneva, vol. 2022, Geneva: United Nations; 2022, URL https://unctad.org/system/files/official-document/rmt2022_en.pdf.

[137] International Maritime Organization. MSC 462 101: Amendments to the international maritime solid bulk cargoes (IMSBC) code. 2019, URL https://wwwcdn.imo.org/localresources/en/KnowledgeCentre/IndexofIMOResolutions/MSCResolutions/MSC.462(101).pdf.

[138] Innofreight Solutions Gmbh. Innofreight DryTainer: New standard for transporting moisture-sensitive bulk goods. 2024, URL https://www.innofreight.com/wp-content/uploads/2023/05/DryTainer_EN.pdf.

[139] NorthStandard. Carriage of direct reduced iron (DRI): Briefing. 2019, URL https://www.google.com/url?sa=t&rct=j&q=&esrc=s&source=web&cd=&ved=2ahUKEwjIiLj8rsODAxWlhf0HHWbPCN8QFnoECBgQAQ&url=https%3A%2F%2Fwww.nepia.com%2Fpublications%2Fcarriage-of-direct-reduced-iron-dri-briefing%2F&usg=AOvVaw1zhpxyjJXlsXYLLNWQwMj0&opi=89978449.

[140] International Iron Metallics Association. Direct reduced iron by-product fines: A guide to handling, storage & shipping. 2020, URL https://www.metallics.org/assets/files/Public-Area/Guides/DRI_Fines_Guide_FinalOct20.pdf.

[141] MAN Energy Solutions. Propulsion trends in bulk carriers. 2022, URL https://www.man-es.com/docs/default-source/marine/tools/propulsion-trends-in-bulk-carriers.pdf?sfvrsn=d851b1c6_14.

[142] Johnston C, Ali Khan MH, Amal R, Daiyan R, MacGill I. Shipping the sunshine: An open-source model for costing renewable hydrogen transport from Australia. Int J Hydrog Energy 2022;47(47):20362–77. http://dx.doi.org/10.1016/j.ijhydene.2022.04.156.

[143] Vignes A, Krietsch A, Dufaud O, Santandréa A, Perrin L, Bouillard J. Course of explosion behaviour of metallic powders - from micron to nanosize. J Hazard Mater 2019;379:120767. http://dx.doi.org/10.1016/j.jhazmat.2019.120767.

[144] Krietsch A, Scheid M, Schmidt M, Krause U. Explosion behaviour of metallic nano powders. J Loss Prev Process Ind 2015;36:237–43. http://dx.doi.org/10.1016/j.jlp.2015.03.016.

[145] Guo Y, Ren K, Wei A, Tao C, Huang W, Zhao P, Wu D. Iron dust explosion characteristics with small amount of nano-sized Fe2O3 and Fe3O4 particles. Fuel 2022;324:124786. http://dx.doi.org/10.1016/j.fuel.2022.124786.

[146] AbdElmomen SS. Reoxidation of direct reduced iron in ambient air. Ironmak Steelmak 2014;41(2):107–11. http://dx.doi.org/10.1179/1743281213Y.0000000105.

[147] Wendel J, Manchili SK, Hryha E, Nyborg L. Reduction of surface oxide layers on water-atomized iron and steel powder in hydrogen: Effect of alloying elements and initial powder state. Thermochim Acta 2020;692:178731. http://dx.doi.org/10.1016/j.tca.2020.178731.

[148] Strauss K. Kraftwerkstechnik. Berlin, Heidelberg: Springer Berlin Heidelberg; 2016, http://dx.doi.org/10.1007/978-3-662-53030-6.

[149] Morris MD. Factorial sampling plans for preliminary computational experiments. Technometrics 1991;33(2):161. http://dx.doi.org/10.2307/1269043.

[150] Francesca Campolongo, Jessica Cariboni, Andrea Saltelli. An effective screening design for sensitivity analysis of large models. Environ Model Softw 2007;22(10):1509–18. http://dx.doi.org/10.1016/j.envsoft.2006.10.004.

[151] Froehling W, Unger H-M, Dong Y. Thermodynamic assessment of plant efficiencies for HTR power conversion systems: (INIS-XA–524). 2002, URL https://inis.iaea.org/collection/NCLCollectionStore/_Public/33/033/33033053.pdf.

[152] Khan MA, Young C, MacKinnon C, Layzell D. The techno-economics of hydrogen compression. 2021, URL https://transitionaccelerator.ca/wp-content/uploads/2023/04/ta-technical-brief-1.1_teea-hydrogen-compression_published.pdf.

[153] Turton R. Analysis, synthesis, and design of chemical processes. Prentice hall PTR international series in the physical and chemical engineering sciences, 3rd ed.. Upper Saddle River N.J.: Prentice Hall; 2009.

[154] Bahadori A. Simple method for estimation of effectiveness in one tube pass and one shell pass counter-flow heat exchangers. Appl Energy 2011;88(11):4191–6. http://dx.doi.org/10.1016/j.apenergy.2011.05.003.

[155] Saleh NS, Alaqel S, Djajadiwinata E, Saeed RS, Al-Suhaibani Z, Zeitoun O, Al-Ansary H, Alswaiyd A, El-Leathy A, Danish S, Jeter S, Byman A, Jordison N, Moon D. Experimental investigation of a moving packed-bed heat exchanger suitable for concentrating solar power applications. Appl Sci 2022;12(8):4055. http://dx.doi.org/10.3390/app12084055.

[156] John E Edwards. Design and rating of shell and tube heat exchangers. 2008, URL http://www.cit-wulkow.chemstations.com/content/documents/Technical_Articles/shell.pdf.

[157] Lange H, Klose A, Beisswenger L, Erdmann D, Urbas L. Modularization approach for large-scale electrolysis systems: a review. Sustain Energy Fuels 2024;8(6):1208–24. http://dx.doi.org/10.1039/D3SE01588B.

[158] Böhm H, Moser S, Puschnigg S, Zauner A. Power-to-hydrogen & district heating: Technology-based and infrastructure-oriented analysis of (future) sector coupling potentials. Int J Hydrog Energy 2021;46(63):31938–51. http://dx.doi.org/10.1016/j.ijhydene.2021.06.233.

[159] María Villarreal Vives A, Wang R, Roy S, Smallbone A. Techno-economic analysis of large-scale green hydrogen production and storage. Appl Energy 2023;346:121333. http://dx.doi.org/10.1016/j.apenergy.2023.121333.

[160] Hodges A, Hoang AL, Tsekouras G, Wagner K, Lee C-Y, Swiegers GF, Wallace GG. A high-performance capillary-fed electrolysis cell promises more cost-competitive renewable hydrogen. Nat Commun 2022;13(1):1304. http://dx.doi.org/10.1038/s41467-022-28953-x.

[161] Manz P, Fleiter T, Eichhammer W. The effect of low-carbon processes on industrial excess heat potentials for district heating in the EU: A GIS-based analysis. Smart Energy 2023;10:100103. http://dx.doi.org/10.1016/j.segy.2023.100103.

[162] Norgate T, Haque N. Energy and greenhouse gas impacts of mining and mineral processing operations. J Clean Prod 2010;18(3):266–74. http://dx.doi.org/10.1016/j.jclepro.2009.09.020.

[163] Müller M, Pfeifer M, Holtz D, Müller K. Comparison of green ammonia and green hydrogen pathways in terms of energy efficiency. Fuel 2024;357:129843. http://dx.doi.org/10.1016/j.fuel.2023.129843.